

# A Bioresorbable and Conductive Scaffold Integrating Silicon Membranes for Peripheral Nerve Regeneration

Pengcheng Sun, Yanjun Guan, Can Yang, Hanqing Hou, Shuang Liu, Boyao Yang, Xiangling Li, Shengfeng Chen, Liu Wang, Huachun Wang, Yunxiang Huang, Xing Sheng, Jiang Peng, Wei Xiong, Yu Wang,\* and Lan Yin\*

Peripheral nerve injury represents one of the most common types of traumatic damage, severely impairing motor and sensory functions, and posttraumatic nerve regeneration remains a major challenge. Electrical cues are critical bioactive factors that promote nerve regrowth, and bioartificial scaffolds incorporating conductive materials to enhance the endogenous electrical field have been demonstrated to be effective. The utilization of fully biodegradable scaffolds can eliminate material residues, and circumvent the need for secondary retrieval procedures. Here, a fully bioresorbable and conductive nerve scaffold integrating N-type silicon (Si) membranes is proposed, which can deliver both structural guidance and electrical cues for the repair of nerve defects. The entire scaffold is fully biodegradable, and the introduction of N-type Si can significantly promote the proliferation and production of neurotrophic factors of Schwann cells and enhance the calcium activity of dorsal root ganglion (DRG) neurons. The conductive scaffolds enable accelerated nerve regeneration and motor functional recovery in rodents with sciatic nerve transection injuries. This work sheds light on the advancement of bioresorbable and electrically active materials to achieve desirable neural interfaces and improved therapeutic outcomes, offering essential strategies for regenerative medicine.

## 1. Introduction

Peripheral nerve injuries (PNIs) are often caused by acute trauma and iatrogenic damage, and can severely impair motor and sensory functions, significantly affecting patients' quality of life.<sup>[1]</sup> There are approximately 300 000 and 360 000 PNI cases per year in Europe<sup>[2]</sup> and the United States respectively,<sup>[3]</sup> and the annual cost of PNI treatments is estimated to be \$1.5 billion in the United States.<sup>[4]</sup> As PNI imposes a significant medical and economic burden on society, there is great interest in developing advanced techniques for improved therapeutic outcomes. For large-gap nerve defects (>1 cm), neuroorrhaphy is not appropriate, and autologous nerve grafting is widely employed as a standard clinical treatment.<sup>[5]</sup> However, donor site morbidity and restricted sources of donor nerves critically limit the use of autograft treatment.<sup>[5]</sup> As an alternative, bioartificial scaffolds have been extensively explored to promote tissue regrowth and functional restoration.

P. Sun, C. Yang, L. Yin  
School of Materials Science and Engineering  
The Key Laboratory of Advanced Materials of Ministry of Education  
State Key Laboratory of New Ceramics and Fine Processing  
Center for Flexible Electronics Technology  
Tsinghua University  
Beijing 100084, P. R. China  
E-mail: lanyin@tsinghua.edu.cn


Y. Guan, B. Yang, X. Li, S. Chen, J. Peng, Y. Wang  
Institute of Orthopedics  
The Fourth Medical Center of Chinese PLA General Hospital  
Beijing Key Lab of Regenerative Medicine in Orthopedics  
Key Laboratory of Musculoskeletal Trauma & War Injuries PLA  
No. 51 Fucheng Road, Beijing 100048, P. R. China  
E-mail: wangyu@301hospital.com.cn

Y. Guan  
Co-innovation Center of Neuroregeneration  
Nantong University Nantong  
Nantong, Jiangsu Province 226007, P. R. China

Y. Guan, B. Yang  
Graduate School of Chinese PLA General Hospital  
No. 28 Fuxing Road, Beijing 100853, P. R. China

H. Hou, S. Liu, W. Xiong<sup>[+]</sup>  
School of Life Sciences  
IDG/McGovern Institute for Brain Research at Tsinghua University  
Tsinghua University  
Beijing 100084, P. R. China

L. Wang  
Key Laboratory of Biomechanics and Mechanobiology of Ministry of Education  
Beijing Advanced Innovation Center for Biomedical Engineering  
School of Biological Science and Medical Engineering  
and with the School of Engineering Medicine  
Beihang University  
Beijing 100083, P. R. China

 The ORCID identification number(s) for the author(s) of this article can be found under <https://doi.org/10.1002/adhm.202301859>

[+] Present address: Chinese Institute for Brain Research, Beijing 102206, China

DOI: 10.1002/adhm.202301859

Scaffolds are mostly made of biodegradable materials, such as collagen<sup>[6]</sup> and poly(L-lactide-co-ε-caprolactone) (PCL),<sup>[7]</sup> to address the issue of potential material residue and postoperative retrieval following tissue regeneration.<sup>[8]</sup> Many efforts have also been made to incorporate bioactive cues or neural precursor cells<sup>[9]</sup> to create an appropriate microenvironment to maximize therapeutic efficacy.<sup>[10]</sup>

Electrical cues are essential bioactive factors that promote nerve regeneration. Increased proliferation of nerve-derived cells and improved recovery of motor functions have been achieved with exogenous electrical stimulation applied to injured nerves,<sup>[11]</sup> such as utilizing an external power source to achieve electrical stimulation (low-frequency nerve or muscle stimulation has been reported to accelerate axon outgrowth and motor functional recovery), self-powered nerve scaffolds utilizing glucose fuel cells, bioresorbable electrical stimulators based on inductive coupling, and self-powered nerve conduits integrating biobatteries such as biodegradable magnesium batteries and zinc-oxygen batteries.<sup>[11e,12]</sup> External electric fields often require external devices or internal self-powered devices, which may pose constraints such as their bulky size, risk of infection, non-degradability, and insufficient stimulation duration. In contrast, an endogenous electric field exists in biological systems and can be leveraged to assist tissue repair by introducing conductive materials that could promote cell adhesion, enhance cellular activity, and facilitate the capture and dissemination of electrical biosignals.<sup>[13]</sup> This type of integrated conductive scaffold offers significant advantages in terms of miniaturization, integration, and continuous electrical stimulation. For example, conductive materials have been shown to upregulate the expression of myelinated genes and the production of neurotrophic factors in Schwann cells,<sup>[14]</sup> accelerate axonal elongation,<sup>[15]</sup> and promote the maturation of neural stem cells by altering the bioelectric properties of cell membranes and enhancing the internal field.<sup>[16]</sup> The charge properties of the material surface also significantly affect cell attachment, and it has been shown that positive charges can improve the adhesion of neural cells.<sup>[17]</sup>

Conductive materials that are often adopted in bioscaffolds for nerve regeneration include polypyrrole (PPY), carbon nanomaterials such as carbon nanotubes (CNTs), carbon nanofibers (CNFs), graphene and graphene oxide (GO),<sup>[18]</sup> polyaniline (PANI), and poly [3,4-ethylene dioxythiophene (EDOT)-co-1,3,5-tri [2-(3,4-ethylene dioxythienyl)]-benzene (EPh)] copolymers (PEDOT-co-EPh),<sup>[18c,19]</sup> among others. For example, PPY shells have been deposited onto electrospun poly(lactide-co-glycolide) (PLGA) fibers to fabricate a conductive nerve conduit,<sup>[20]</sup> PEDOT is deposited on the inside of a soft thermosensitive agarose hydrogel conduit to create a conductive scaffold,<sup>[21]</sup> graphene oxide (GO) and gelatin-methacrylate (GelMA) composites have been realized to build conductive nerve conduits to repair nerve

defects,<sup>[22]</sup> and anisotropic conductive conduits made from coaxially aligned carbon nanotube-modified electrospun PCL-collagen scaffolds have been used to repair nerve defects.<sup>[23]</sup> Combining electrical stimulation with conductive conduits prepared by depositing PPY on 3D-bioprinted silk fibroin scaffolds has also been demonstrated to be effective in promoting nerve repair.<sup>[11a]</sup> Achieving a fully bioresorbable and conductive nerve scaffold can offer additional advantages for nerve regeneration by eliminating material retention and avoiding the need for a secondary retrieval surgery.<sup>[8]</sup>

Given their excellent biodegradability and biocompatibility, Si membranes could serve as desirable conductive components for regenerative medicine. Si membranes represent essential constituents for high-performance biodegradable electronics and can degrade in biofluids at different rates ranging from a few nanometers to several hundreds of nanometers per day, depending on doping levels, geometry, and associated biological environments.<sup>[24]</sup> The hydrolysis product of Si is silicic acid  $\text{Si}(\text{OH})_4$  ( $\text{Si} + 4 \text{H}_2\text{O} \leftrightarrow \text{Si}(\text{OH})_4 + 2 \text{H}_2$ ),<sup>[25]</sup> which is a naturally occurring component in biofluid, for example, the typical concentration in serum is approximately 14–39  $\mu\text{M}$ .<sup>[26]</sup> Studies have suggested the desirable biocompatibility of degradation byproducts of Si in physiological environments.<sup>[27]</sup> For example, studies have shown that when Si nanoparticles are injected into the blood of rats, traces of these nanoparticles can be found in the liver, kidneys, and spleen. One day later, macrophages were found in the liver, indicating that the nanoparticles were naturally engulfed and degraded. After four weeks, all tissues returned to normal, and throughout the process, the organs maintained their normal morphology.<sup>[28]</sup> Biochemical studies of the biodistribution of degraded Si membranes also indicate minimal abnormal accumulation of Si in major organs after 7 weeks and no significant adverse effects.<sup>[27b]</sup> Moreover, the byproduct silicic acid is a fundamental component of the human body,<sup>[26]</sup> and excess silicic acid in human blood can be quickly absorbed by the kidneys and expelled through urine.<sup>[29]</sup>

Furthermore, micropillar arrays of Si can guide the axon growth of hippocampal neurons without inducing significantly adverse effects.<sup>[30]</sup> By introducing an appropriate amount of dopants, the resistivity of the Si membrane can reach 0.01–0.025  $\Omega\text{-cm}$ , a conductivity level that is beneficial for axonal growth.<sup>[13c,20,31]</sup> In addition, previous studies have shown that as cell membranes are negatively charged, cells settle and adhere more quickly to substrates with a positive charge, resulting in the preferred formation of neural networks at the point of deposition.<sup>[17,32]</sup> In aqueous solution, N-type Si has a positively charged surface, whereas P-type silicon has a negatively charged surface.<sup>[24a]</sup> N-type Si could therefore serve as a desirable neural interface and potentially enhance endogenous electrical cues to promote nerve regeneration. However, the incorporation of flexible and conductive N-type Si membranes with nerve scaffolds has rarely been explored before.

Here, we propose a fully biodegradable conductive nerve conduit integrating N-type Si membranes to enhance the conduction of endogenous electric fields (**Figure 1a**). The scaffold consists of conductive N-type Si membranes on a polymer-based biodegradable conduit with directional electrospun fibers, which simultaneously offers structural guidance and enhanced endogenous electrical cues. The presence of N-type Si membranes enhances

H. Wang, Y. Huang, X. Sheng  
Department of Electronic Engineering  
Beijing National Research Center for Information Science and Technology  
Institute for Precision Medicine  
Center for Flexible Electronics Technology  
and IDG/McGovern Institute for Brain Research  
Tsinghua University  
Beijing 100084, China

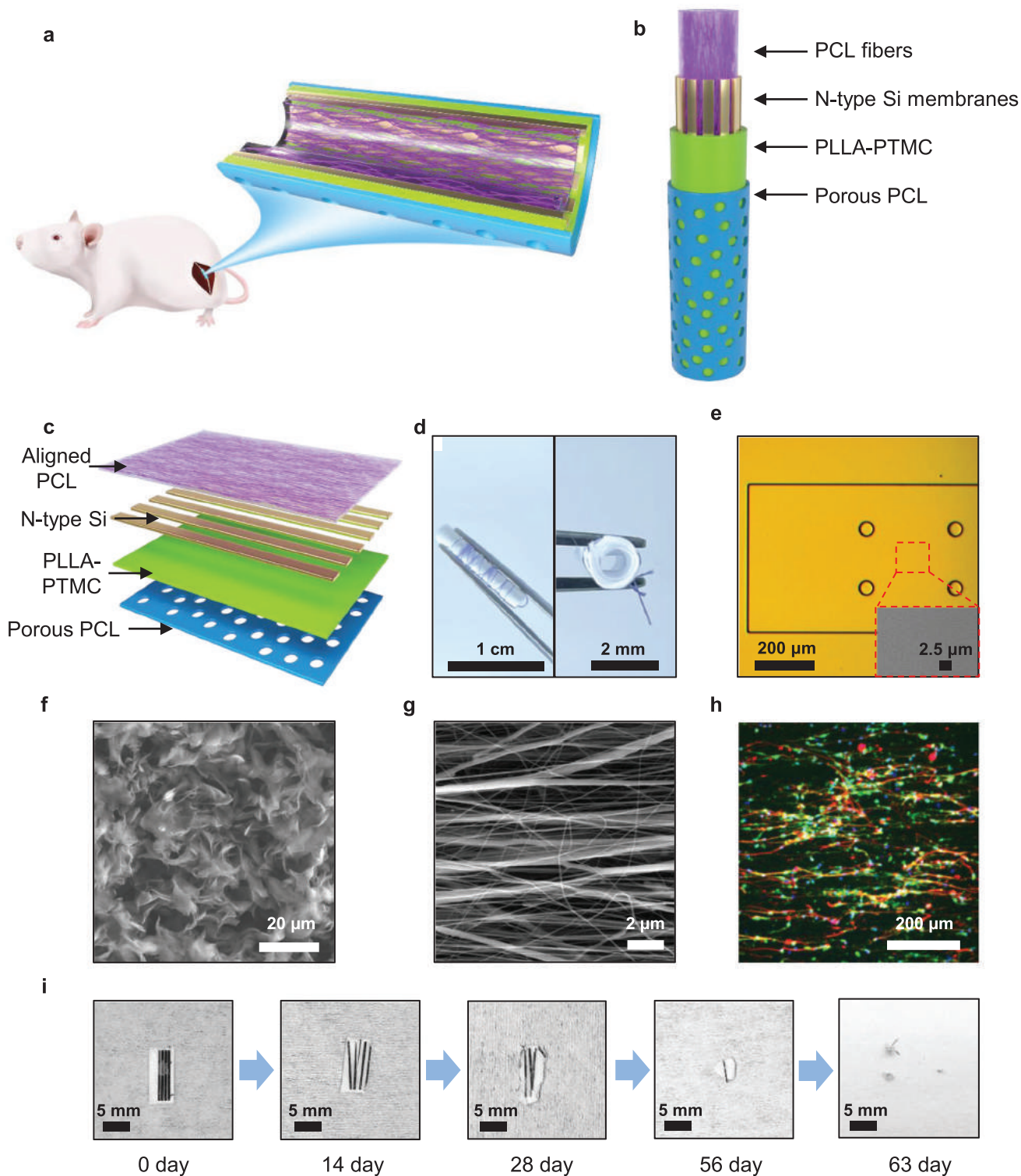


**Figure 1.** A bioresorbable and conductive nerve conduit for neuroregenerative medicine. a) Schematic illustration of the bioresorbable and conductive conduit for sciatic nerve regeneration. b) Schematic exploded illustration of the conduit composed of a porous PCL layer ( $\approx 350 \mu\text{m}$ ), a PLLA-PTMC layer ( $\approx 200 \mu\text{m}$ ), N-type Si membranes ( $\approx 5 \mu\text{m}$ ), and electrospun PCL fibers ( $\approx 30 \mu\text{m}$ ). c) Multilayer structure of the conduit before rolling. d) Photo of the conduit: front view (left) and side view (right). e) Optical image of the N-type Si membrane. An array of holes ( $50 \mu\text{m}$  in diameter) is made to accelerate the undercut of buried oxide by hydrofluoric acid and facilitate the transfer printing process of Si membranes from the SOI wafers. Inset: SEM image of the N-Type Si membrane, indicating a smooth surface. f) SEM image of the porous PCL layer. g) SEM image of electrospun directional PCL fibers. h) SEM image of the conduit showing the porous PCL layer, PLLA-PTMC layer, N-type Si membranes, and electrospun PCL fibers. i) Time-lapse photos of the conduit at 0 day, 14 day, 28 day, 56 day, and 63 day, showing the degradation of the conduit over time.

the calcium activity of dorsal root ganglion (DRG) neurons and promotes the proliferation and secretion of neurotrophic factors in Schwann cells. Accelerated tissue regeneration and enhanced motor functional recovery are achieved by the conductive scaffold in Sprague-Dawley (SD) rats with sciatic nerve transection injuries (10 mm gap), suggesting improved therapeutic efficacy introduced by conductive Si membranes. The scaffold is fully degradable, which can effectively reduce material residues and alleviate the need for a secondary surgical procedure for removal. Fully biodegradable and conductive nerve scaffolds have rarely been reported before. Considering the slow degradation rate of the conductive silicon membranes, it is possible that the conductive nerve conduit can offer a long-lasting electric cue. This work provides new routes toward the development of fully bioresorbable and electrically active materials and achieves desirable biological microenvironments, offering important strategies for neural interface engineering in regenerative medicine.

## 2. Results

### 2.1. Materials Strategies and Fabrication Schemes

The schematic structure of the biodegradable and conductive nerve scaffold appears in Figure 1b, with the corresponding planar view shown in Figure 1c. The nerve scaffold is composed of single crystalline N-type Si membranes embedded in a biodegradable polymeric conduit, which has a bilayer structure comprising porous PCL and a copolymer of poly(L-lactic acid) and poly(trimethylene carbonate) (PLLA-PTMC). Directional PCL fibers are electrospun on N-type Si membranes as the inner layer of the conduit. A photograph of the scaffold is shown in Figure 1d, and the associated fabrication process is illustrated in Figure S1a, Supporting Information. Figure 1e shows an optical image of the N-type Si membrane, with the scanning electron microscope (SEM) image in the inset, indicating the smooth surface of N-type Si (Figure S1c, Supporting Information). To accelerate the undercutting of buried oxide in silicon-on-insulator (SOI) by hydrofluoric acid (HF) and facilitate the transfer printing process of N-type Si membranes, an array of holes was made on patterned Si ribbons through photolithography (Figure S1b, Supporting Information). The structural influence of N-type Si membranes on the growth of nerve cells is expected to be minimal compared to that of other microstructures, such as directional nanofibers. This is because DRG neurons have axon diameters that typically range between 2 and 6  $\mu\text{m}$ , significantly smaller than the feature size of Si membranes.<sup>[33]</sup>

The outer porous PCL film (thickness  $\approx 350 \mu\text{m}$ ) (Figure 1f) is formed via a salt-etching method, providing mechanical support and the permeability of nutrition factors. The flexible and highly stretchable PLLA-PTMC film (thickness  $\approx 200 \mu\text{m}$ ) serves as the next layer offering a desirable soft interface in contact with nerve tissues. Positively charged surfaces have been shown to facilitate the settlement process of cell suspensions and therefore promote the adhesion of neuronal cells,<sup>[17]</sup> while P-type silicon sur-

faces with negative charges have been reported to hinder the adhesion of DRG neuron axons.<sup>[34]</sup> To realize desirable neural interfaces, N-type Si membranes (thickness  $\approx 5 \mu\text{m}$ ,  $0.06\text{--}0.09 \Omega \text{ cm}$ ) with positively charged surfaces were therefore adopted as the conductive path connecting the proximal and distal ends of the sciatic nerve, which were achieved by releasing the N-type Si ribbons from the host SOI wafer and transfer-printing onto the PLLA-PTMC surface (Figure S1a, Supporting Information). Previous studies have shown that micron-sized Si films combined with flexible substrates can achieve flexibility and conformal contact.<sup>[35]</sup> The optical images of Si membranes on polymeric substrates remain intact before and after rolling with no visible breakage (Figure S1d, Supporting Information). Moreover, the conductivity of the Si membranes used in our conductive conduits is greater than that of traditional conductive conduits utilizing conductive polymers (e.g., PPy, PEDOT).<sup>[36]</sup> The ultrathin electrospun PCL fibers (thickness  $\approx 30 \mu\text{m}$ ) serve as the inner layer of the conduit to provide topographical guidance for nerve regrowth. The highly aligned morphology of PCL fibers appears in Figure 1g. DRG neurons cultured on aligned PCL fibers demonstrated directed axonal growth along the same direction, indicating effective structural guidance (Figure 1h). The conductive conduit is fabricated in a planar format, and subsequent rolling of the multilayer structure yields a three-dimensional (3D) scaffold (Figure S1a, Supporting Information).

The degradation characteristics of the conductive scaffold in a planar format were investigated in phosphate-buffered saline (PBS) solution (pH 7.4,  $55^\circ\text{C}$ ), and the images at different degradation stages are shown in Figure 1i. The results demonstrate the disintegration, fracturing and dissolution of Si ribbons accompanied by the hydrolyzation of polymeric conduits. By approximately two months, the conductive scaffold is almost completely degraded, and only ultrafine fragments of Si and polymeric components can be filtered from PBS solutions (Figure 1i). The degradation and conductivity changes of the N-type Si film in PBS under accelerated conditions ( $55^\circ\text{C}$ ) are shown in Figure S2, Supporting Information. Our results show a gradual dissolution of the N-type Si membrane, with a degradation rate of 13 nm/day, which is consistent with previously reported degradation of Si membranes.<sup>[37]</sup> The overall resistivity of N-type Si remains almost constant in the first 3 weeks due to the slow degradation rates, which is advantageous for providing continuous electrical cues to promote nerve regrowth.

### 2.2. In Vitro Cell Growth Behavior

Schwann cells and DRG neurons were cultured with N-type Si to investigate the influence on cell proliferation and axonal growth. The resistivity of N-type Si is measured to be  $0.06\text{--}0.09 \Omega \text{ cm}$ . Representative fluorescence images of Schwann cells cultured on N-type Si (N-type group) and tissue culture polystyrene (TCPS, control group) demonstrating cell proliferation on Day 3 are shown in Figure 2a. In the presence of N-type Si, Schwann cells

Confocal microscope image of guided neurite outgrowth of dorsal root ganglion (DRG) neurons cultured on aligned electrospun PCL fibers on day 7, with immunohistochemical staining for axons ( $\beta$ -Tubulin, green), Schwann cells (S100, red), and nuclei (4', 6-diamidino-2-phenylindole (DAPI), blue). i) Images of the degradation process of the bioresorbable and conductive conduit (in the planar state) at various stages in phosphate buffered saline (PBS, pH = 7.4) at  $55^\circ\text{C}$ . In h,  $n = 5$  independent experiments.

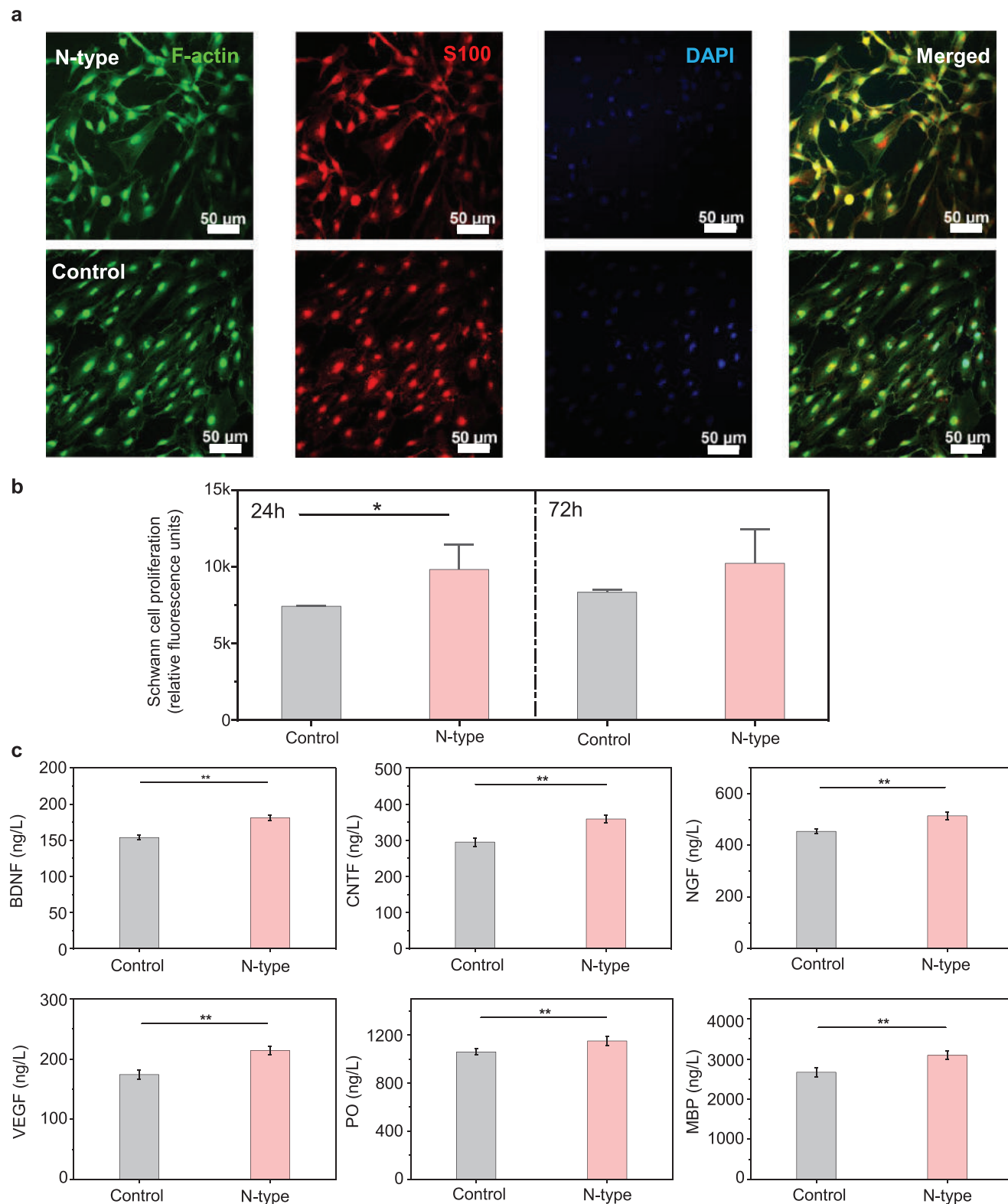


**Figure 2.** The influence of conductive N-type Si on the behavior of Schwann cells. a) Immunostaining images of the proliferation of Schwann cells in the N-type and control groups on day 3. Immunofluorescence staining: Cytoskeleton (F-actin, green), Schwann cells (S100, red), and nuclei (DAPI, blue). b) Proliferation assay of Schwann cells using the alamarBlue. c) Enzyme-linked immunosorbent assay (ELISA) of BDNF, CNTF, NGF, VEGF, PO and MBP production in Schwann cells of the N-type and control groups on day 1.  $n = 4$  independent experiments. Data are mean  $\pm$  standard deviation (\*  $p < 0.05$ , \*\*  $p < 0.01$ ).

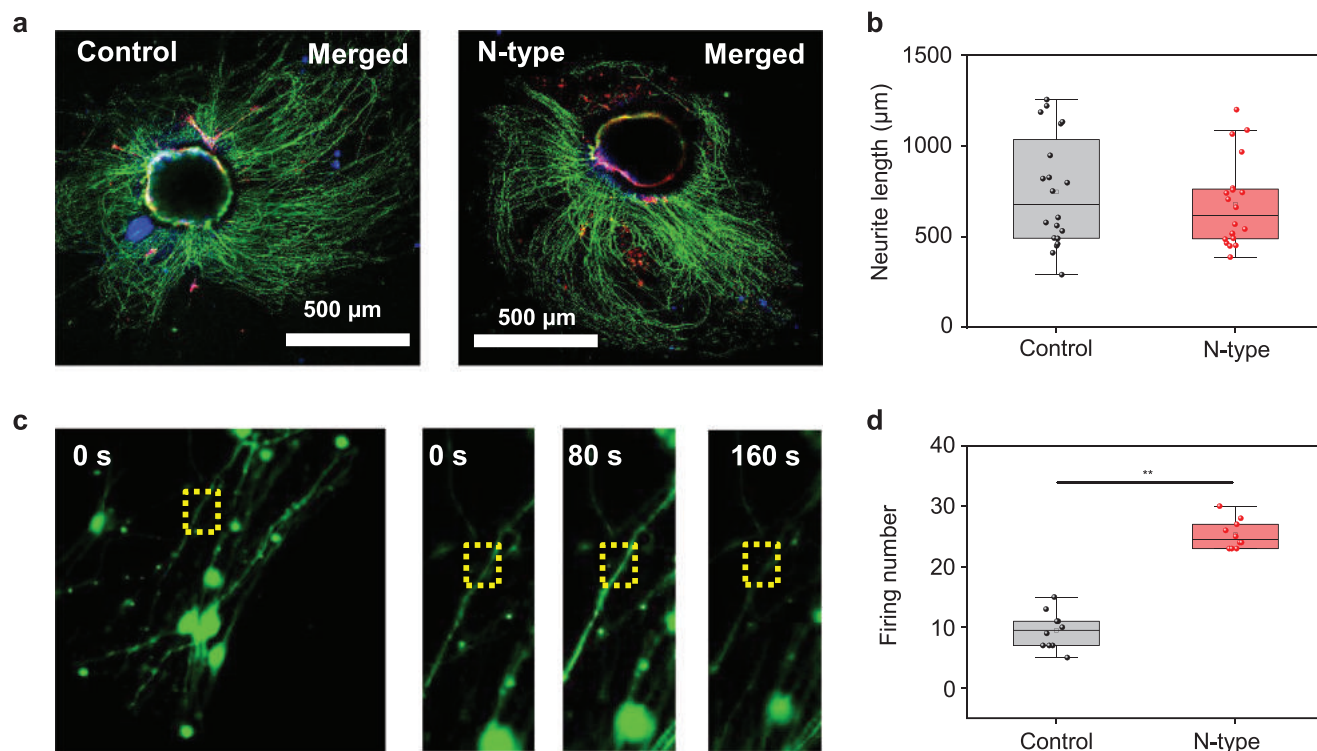


**Figure 3.** The influence of conductive N-type Si on the behavior of DRG neurons. a) Immunostaining images of DRG neurons cultured with N-type Si (N-type group) and glass (control group) on day 7, with immunohistochemical staining for axons (β-Tubulin, green), Schwann cells (S100, red), and nuclei (DAPI, blue). b) Statistical analysis of the neurite length of DRG neurons in the control group and N-type group. c) Time series images of calcium dynamics of the DRG neurons in the N-type group. d) Quantification of the number of calcium waves within 120 s in 10 DRG neuronal axons of the N-type and control groups. In a and b,  $n = 3$  independent experiments. Data are mean  $\pm$  standard deviation ( $* p < 0.05$ ,  $** p < 0.01$ ).

demonstrated significantly enhanced proliferation ( $P < 0.05$ ) after 24 h, while the difference gradually disappeared after 72 h (Figure 2b). The concentration of six neurotrophic factors, including brain-derived neurotrophic factor (BDNF), ciliary neurotrophic factor, nerve growth factor (NGF), vascular endothelial growth factor (VEGF), myelin protein zero (P0) protein and myelin basic protein (MBP), in the supernatant of the culture medium of Schwann cells at 24 h was analyzed by enzyme-linked immunosorbent assay (ELISA). The results show that the neurotrophic factors are all upregulated in the presence of N-type Si ( $P < 0.01$ ) (Figure 2c). The enhanced production of neurotrophic factors was also observed at 72 h, except for VEGF (Figure S3, Supporting Information), suggesting the promoted capability of angiogenesis and myelin sheath formation which are beneficial for nerve regeneration. Gene Ontology (GO) analysis was performed on Schwann cells on Day 3 in the N-type and control groups (Figure S4, Supporting Information), and the results showed that the expression of regeneration-related genes, such as regeneration and animal organ regeneration genes, was significantly increased in the N-type group compared with the control group, which is consistent with the ELISA results. The genomic results also reveal greater expression of genes associated with cell attachment in the N-type group, such as basement membranes and extracellular matrix, which suggests that N-type Si with a positively charged surface could be beneficial to improve cell adhesion. As N-type Si demonstrates a positive influence on cell adhesion and the production of neurotrophic factors in Schwann

cells at the initial stage (first 24–72 h), it could play a critical role in assisting the differentiation, proliferation, and migration of Schwann cells to form bands of Bungner and guide subsequent axonal growth.<sup>[34]</sup>

The growth behavior of DRG neurons was also explored. N-type Si (N-type group, resistivity 0.06–0.09  $\Omega$ -cm) and glass (control group) were cultured with DRG neurons to evaluate the influence of N-type Si on nerve regeneration, and the immunofluorescence images on Day 7 are shown in Figure 3a. Although the smooth surface of intrinsic Si has been considered to be detrimental to cell adhesion,<sup>[38]</sup> the axonal growth of neurons on smooth N-type Si is comparable to that of the control group (Figure 3b). As the regulation of neurite growth and motility is closely associated with cellular calcium ( $\text{Ca}^{2+}$ ) dynamics,<sup>[39]</sup> the calcium activity of the DRG neuron network in the N-type and control groups was further evaluated. Time series images of a calcium wave in the region of the DRG neuron axon in the N-type group are shown in Figure 3c. To quantify the calcium activity, the regions of 10 axons are selected from each group to count the firing number of calcium activity over 120 seconds, and the results are shown in Figure 3d and Movies S1, Supporting Information. The statistical results indicate that N-type Si with greater conductivity induces stronger calcium activity within the DRG network compared with the control group ( $P < 0.01$ ). The enhanced calcium activity plays an important role in pathfinding and cue-sensing activity at the end of axons,<sup>[39,40]</sup> encouraging neurite growth. Nevertheless, due to the increased hydropho-

bicity of smooth Si surfaces compared to glass surfaces,<sup>[41]</sup> the adhesion of DRG can be impeded, which, in turn, affects axonal growth as reported before.<sup>[42]</sup> Under the combined effect of these two factors, there was no observed significant difference in axonal length between the DRG cells on the surface of N-type Si and the control group in the in vitro studies. To address the potential adhesion issues and further promote the positive effects of conductive Si membranes, structural guidance, such as the directional polymeric fibers incorporated in our conductive scaffolds, can be introduced on the surface of Si membranes for in vivo investigation. Overall, N-type Si can significantly upregulate neurotrophic factors, stimulate the proliferation of Schwann cells at the early stage, and improve the calcium activity of DRG neurons, which are all favorable for nerve regeneration.

### 2.3. Evaluation of Nerve Regeneration In Vivo

To evaluate the efficacy on nerve regrowth, the bioresorbable and conductive nerve scaffolds with N-type Si membranes (N-type group) are implanted in the transected sciatic nerve (10 mm gap) of the right limb in SD rats. Autologous grafting (autograft group) and the scaffold without Si membranes (control group) were also investigated for comparison (Figure S5, Supporting Information). Notably, the ultrathin electrospun PCL films were also present in the control group.

The regenerated nerves were collected at 3 weeks and 12 weeks postoperatively. No significant inflammation was observed surrounding the implantation site within the experimental window. All scaffolds undergo partial degradation on week 3, mostly resulting from the breakdown of the outer porous PCL layer, while the PLLA-PTMC layer remains almost intact after 12 weeks, ensuring minimal mechanical deformation of the scaffold. Given the slow degradation rate of N-type Si, conductive pathways could remain functional until nerve repair is complete. Longitudinal sections of regenerated nerve tissues at 3 weeks after implantation and transverse sections of regenerated tissues at 12 weeks after implantation were investigated. Representative immunofluorescence images at week 3 are shown in Figure 4a and Figure S6–S8, Supporting Information, and the statistical quantification of regeneration axon length is shown in Figure 4d. The results revealed that the conductive scaffold accelerated nerve regrowth at the early stage compared with the control group (Figure 4d,  $P < 0.01$ ). Moreover, from the longitudinal section results, it can be observed that the scaffold materials remained present around the regenerated neural tissues at 3 weeks. Further examination of the retrieved nerve segments demonstrated that there was no significant degradation of the conduit at 3 weeks. Hematoxylin and eosin (H&E) staining images are illustrated in Figure S9, Supporting Information, demonstrating no significant inflammation.

Transverse sections of regenerated nerve tissues at 12 weeks postoperatively were obtained to investigate the myelinated axon fibers in detail. We performed histological studies, including toluidine blue staining of regenerated nerves located at the distal end of the nerve segments (Figure 4b) and transmission electron microscopy (TEM) characterization of transverse sections at the middle of the regenerated nerve segments (Figure 4c), to reveal the distribution, density, and morphology of the myelin sheath.

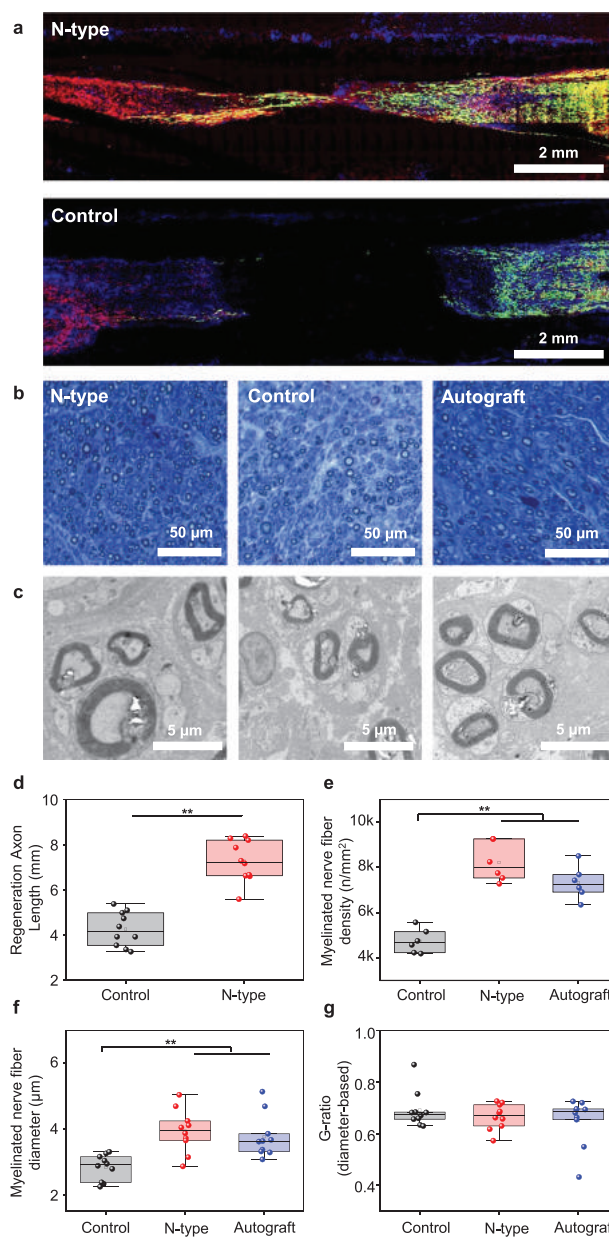


**Figure 4.** Evaluations of regenerated nerve segments at 3 and 12 weeks after implantation of the N-type, control, and autograft groups. a) Immunofluorescent images of the longitudinal sections of regenerated nerve tissues at 3 weeks after implantation of the N-type and control groups. Immunohistochemical staining: axons (NF200, green), Schwann cells (S100, red), and nuclei (DAPI, blue). b) Toluidine Blue staining of regenerated nerves located at the distal end of nerve segments on week 12. c) TEM images of the transverse sections at the middle of the regenerated nerve segment on week 12. d) Regeneration axonal length of regenerated nerves on week 3. e) Myelinated nerve fiber density of the transverse sections at the middle of the regenerated sciatic nerves on week 12. f) Myelinated nerve fiber diameter of the transverse sections at the middle of the regenerated sciatic nerves on week 12. g) Average diameter-based g-ratio.  $n = 5$  (week 3) and  $n = 6$  (week 12) independent experiments. Data are mean  $\pm$  standard deviation (\*  $p < 0.05$ , \*\*  $p < 0.01$ ).

The toluidine blue staining images (Figure 4b) and associated statistical results (Figure 4e) indicated that the regenerated myelinated nerve fibers in the N-type group were evenly distributed with greater density than in the control group ( $P < 0.01$ ), and were similar to those in the autograft group, implying a higher degree of myelination. The myelinated nerve fiber diameter and G-ratio (diameter-based) were quantified by analyzing the TEM images (Figure 4c). The results suggest that although there is no significant difference in the G-ratio in all the groups, the averaged diameter of regenerated myelinated nerve fibers in the N-type group is significantly greater than that in the control group ( $P < 0.01$ ), and there is no significant difference compared with the autograft group (Figure 4f,g). The myelinated nerve fibers in the N-type group and autograft groups also demonstrated better uniformity and consistent morphology than those in the control group. These results suggest that the conductive scaffold offers a positive effect on nerve growth and remyelination.

## 2.4. Evaluation of Motor Function Recovery

As the degree of functional recovery is an important index for assessing nerve regeneration, gastrocnemius muscle atrophy evaluation, electrophysiological assessment, and walking track analysis were performed at 12 weeks after implantation. Regeneration of transected nerve tissues can establish reinnervation to muscles, which will otherwise cause muscle atrophy. The evaluation of gastrocnemius muscle atrophy was performed by measuring the muscle wet weight and the cross-sectional area of muscle fibers. Representative gross images of the gastrocnemius muscles of injured (right) and contralateral (left) hindlimbs in the N-type, control, and autograft groups are shown in Figure 5a. Muscles of the N-type and autograft groups showed lower levels of atrophy than those of the control group. The ratio of the muscle wet weight of the injured side to that of the contralateral side was analyzed to quantify the degree of atrophy, and the results are shown in Figure 5c. The muscle-wet weight of the N-type group was significantly higher than that of the control group ( $P < 0.05$ ), while the muscle-wet weight of the autograft group was significantly higher than that of the N-type and control groups ( $P < 0.01$ ). Figure 5b shows representative Masson's trichrome staining images of transverse sections of gastrocnemius muscles from the injured side. Compared with the control group, the muscle fibers of the gastrocnemius in the N-type group and autograft group were distributed in a regular manner, indicating a better recovery. Based on Masson's trichrome staining images, the area of muscle fibers from the injured side was measured and the statistical results are shown in Figure 5d. The results show that the muscle fiber area in the N-type group was significantly higher than that in the control group ( $P < 0.01$ ), indicating less muscle atrophy.

During the course of nerve regeneration, the innervation of nerve to muscle tissue is gradually restored. By electrically stimulating the proximal end of the sciatic nerve at the injured side (operated), the compound motor action potential (CMAP) is recorded at the target gastrocnemius muscles to evaluate the recovery of nerve conduction. To ensure the consistency of the assessment and minimize the influence resulting from the variation of different animals, the CMAP of the contralateral side

(unoperated) was also measured, and the ratio of latency time (Figure 5e) and amplitude (Figure 5f) of the injured side to the contralateral side is summarized in Figure 5e and Figure 5f. Although there was no significant difference in CMAP amplitude for all groups, the CMAP latency time of the N-type group was similar to that of the autograft group and was significantly reduced compared with that of the control group ( $P < 0.05$ ), demonstrating that conductive conduits assist the reinnervation of muscle tissues. Based on the electrophysiological assessment, accelerated nerve reinnervation to the muscle was achieved in the N-type group compared with the control group, which could be attributed to the provided conductive pathway to promote nerve regrowth and maturation.

Different levels of muscle atrophy caused by injured nerves could deform the position of toes,<sup>[43]</sup> resulting in shortened toe spread, and intermediate toe spread, and a lengthened footprint.<sup>[44]</sup> Gait analysis is therefore a key assessment of motor functional recovery. A CatWalk system was used to evaluate the gait of the SD rats every 3 weeks after implantation. The sciatic functional index (SFI) based on footprints was calculated to quantify gait results. The representative 3D plantar pressure distribution of the right (injured side) and left (contralateral side) hindlimbs of SD rats at 12 weeks after implantation is illustrated in Figure 6a. In the 3D plantar pressure distribution images, the x-axis and y-axis represent the length and width of the footprint, respectively, and the z-axis represents the relative intensity of scattered light on the plantar, which is correlated with the plantar pressure. The results suggest that the footprint area and pressure distribution of the N-type group are close to those of the autograft group. The SFI results are summarized in Figure 6b. The closer the SFI value is to 0, the better the recovery, while SFI values close to  $-100$  demonstrate serious dysfunction. In all cases, the SFI values dropped sharply for all groups immediately after the surgery and remained at low values during the first 3 weeks, followed by a gradual increasing trend during the course of nerve regeneration. The SFI values in the N-type group were significantly higher than those in the control group at 6 and 9 weeks ( $P < 0.01$ ) and 12 weeks ( $P < 0.05$ ) after implantation, while there was no significant difference between the N-type group and the autograft group, suggesting that the bioresorbable and conductive scaffold can boost the recovery of motor function.

## 3. Conclusions

We propose a new type of bioresorbable and conductive nerve scaffold integrating N-type Si membranes with biodegradable polymer conduits to promote peripheral nerve regeneration. The entire scaffold can be completely biodegradable in the physiological environment, which effectively reduces material residuals and eliminates the need for a secondary surgery to remove it. The presence of conductive N-type Si membranes has been shown to improve the proliferation of Schwann cells and the production of neurotrophic factors at the early stage. The positively charged N-type Si membranes can also boost the calcium activity of DRG neurons, which could be attributed to the modulated cell membrane properties and enhanced endogenous electric field. The bioresorbable and conductive scaffold successfully accelerates tissue regeneration and motor functional recovery in rodents with sciatic nerve injuries (10 mm gap). Future work includes fabricat-



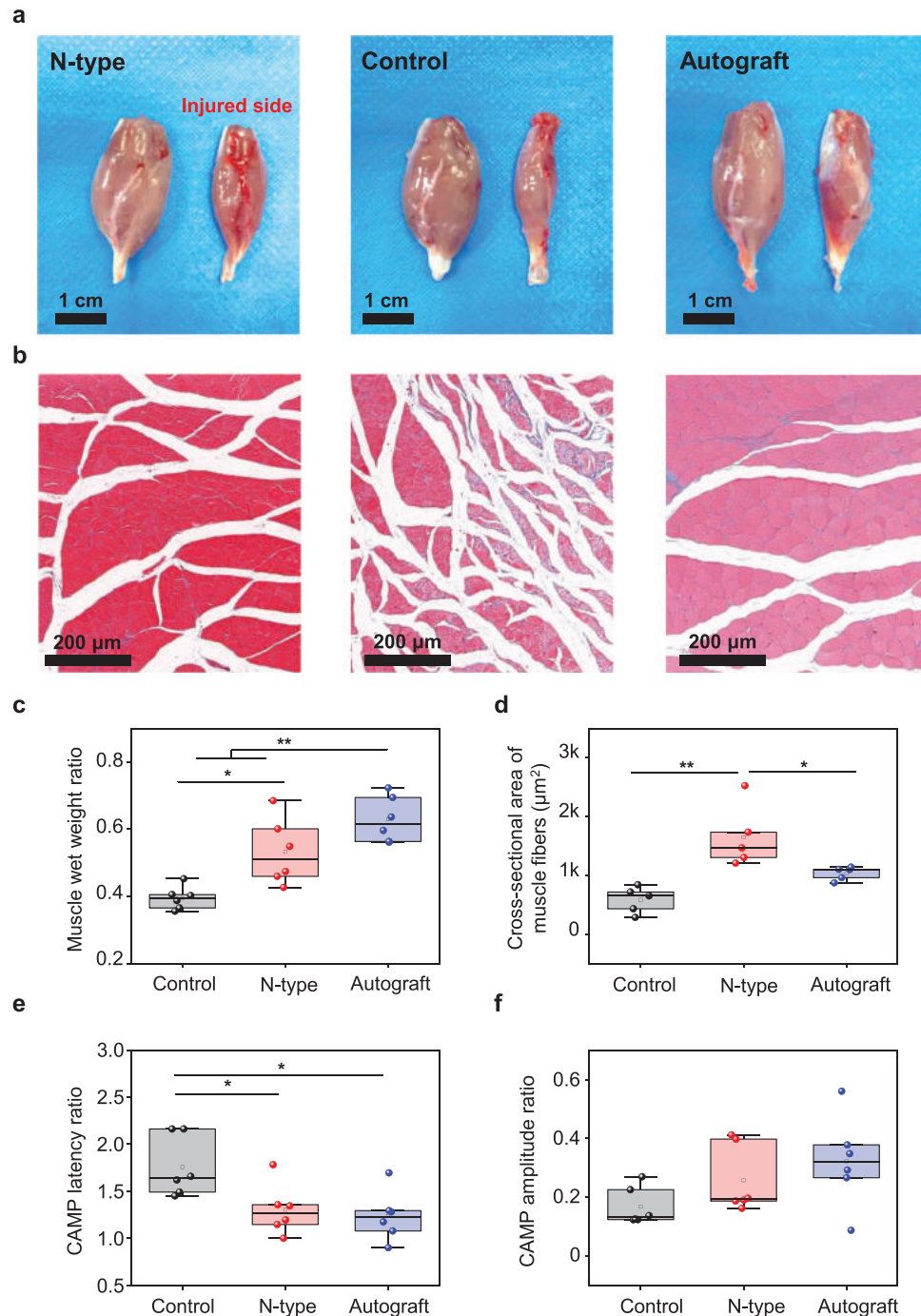


**Figure 5.** Evaluation of gastrocnemius muscles atrophy and reinnervation at 12 weeks postoperatively of the N-type, control, and autograft groups. a) Gross images of the gastrocnemius muscles of the injured side (right) and contralateral side (unoperated, left). b) Masson's trichrome staining images of the transverse sections of gastrocnemius muscles from the injured side. c) Statistical results of the wet weight ratio of the gastrocnemius muscles of the injured side to the contralateral side. d) Statistical results of the area of muscle fibers from the injured side based on Masson's trichrome staining images. e) Statistical results of CMAP latency ratio of the injured side to the contralateral side. f) Statistical results of CMAP amplitude ratio of the injured side to the contralateral side. In a, c, e, and f,  $n = 6$  independent animals per group. In b and d,  $n = 5$  independent animals per group. Data are mean  $\pm$  standard deviation (\* $p < 0.05$ , \*\* $p < 0.01$ ).

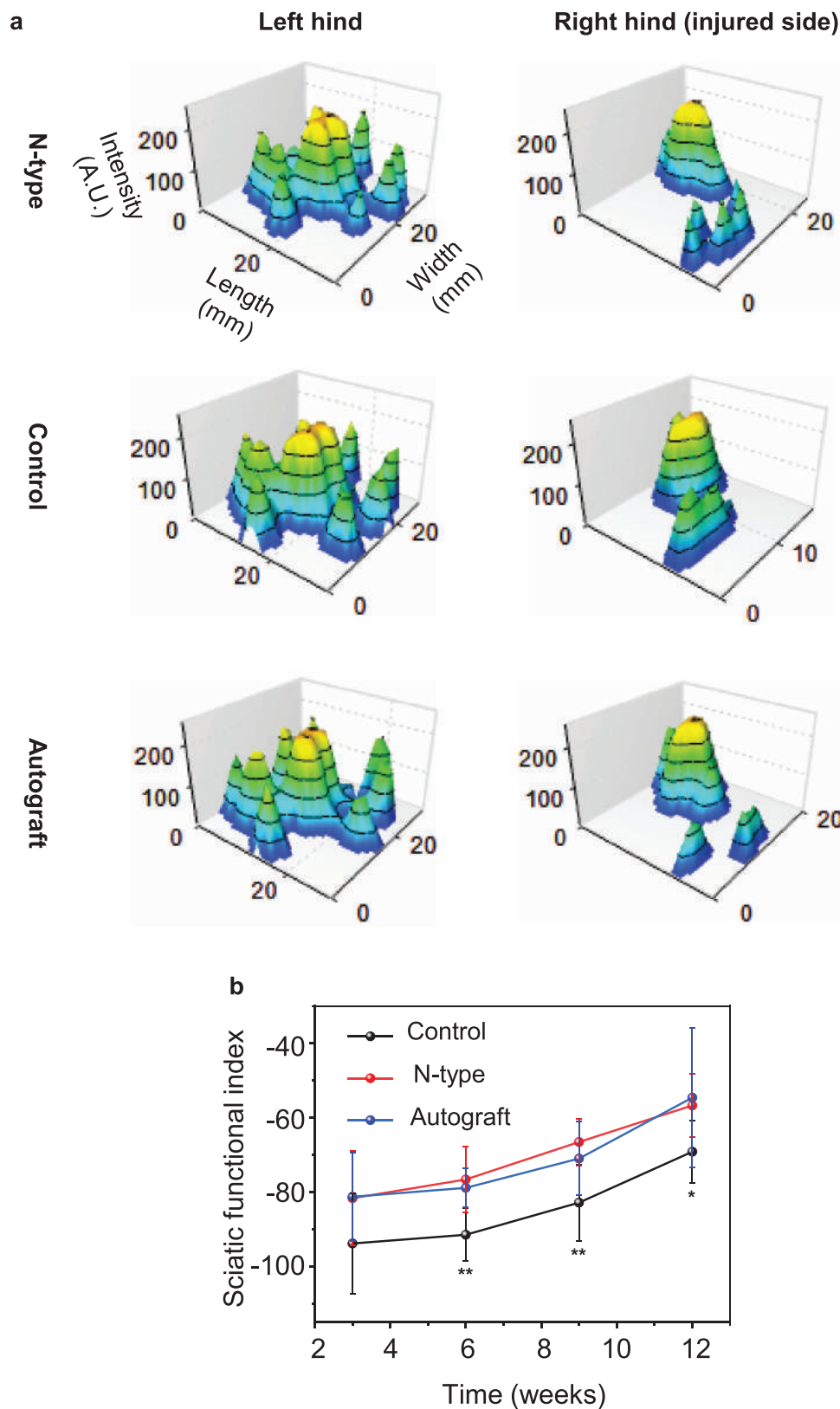


**Figure 6.** Assessment of the motor functional recovery of the N-type, control, and autograft groups. a) Representative 3D plantar pressure distribution of walking track of SD rats at 12 weeks postimplantation. A.U. stands for arbitrary units. b) SFI values. For each group,  $n = 11$  for week 3,  $n = 6$  for weeks 6 and 9, and 12. Data are mean  $\pm$  standard deviation (\*  $p < 0.05$ , \*\*  $p < 0.01$ ).

ing 3D conductive pathways based on Si membranes to achieve a better modulation of the electric network and combining the conductive interface with bioresorbable self-powered sources to enhance electrical cues. Advanced micro- and nanofabrication techniques enable the fabrication of Si into devices of diverse forms and sizes. As Si has been extensively explored for neural sensing,<sup>[45]</sup> opto-thermal applications,<sup>[46]</sup> and optoelectronic stimulation,<sup>[47]</sup> the integration of functional Si devices with scaffold materials can potentially enable multifunctional devices that can maximize therapeutic outcomes. Overall, this work promotes the development of bioresorbable and conductive neural interfaces to create biomimetic microenvironments that are beneficial for regenerative medicine.

## 4. Experimental Section

**Fabrication of Silicon Membranes:** SOI wafers (device layer, N-type, 5  $\mu\text{m}$ , 0.01–0.025  $\Omega\text{-cm}$ ; handle layer, N-type, 525  $\mu\text{m}$ , 20–30  $\Omega\text{-cm}$ ; buried oxide, 500 nm) were purchased from Topvender (Beijing Topvender Technology Co., Ltd.). Fabrication was carried out using standard lithographic processes (photoresist SPR220-v3.0,  $\approx 1 \mu\text{m}$ , Rohm & Haas, Philadelphia, PA, USA) and reactive-ion etching ( $\text{SF}_6$  plasma, 150 sccm, 80 mTorr, 100 W, etching rate  $\sim 1 \mu\text{m}/\text{min}$ ). The device layers were patterned into ribbons (10 000  $\mu\text{m} \times 500 \mu\text{m}$ ) with arrays of holes (50  $\mu\text{m}$  in diameter) (Figure S1b, Supporting Information) to assist the undercut etching of buried oxides using HF. The array of N-type Si membranes was subsequently transferred onto a PLLA-PTMC layer by heat release tape.

**Fabrication of Biodegradable and Conductive Nerve Scaffolds:** PLLA-PTMC (60:40, viscosity of 2.2 mPa·s; Jinan Daigang Biomaterial Co. Ltd., China) was dissolved in chloromethane ( $\text{CHCl}_3$ ) (Beijing Tongguang Chemical Co. Ltd., China) in a weight-to-volume (w/v) ratio of 1:10, followed by drop-casting (4 mL of the precursor solution) on a glass slide and curing for 12 h at 4 °C to achieve PLLA-PTMC films (thickness: 200  $\mu\text{m}$ ; size: 4.7 mm  $\times$  10 mm). Sodium chloride (NaCl) was mixed with PCL in a weight-to-weight (w/w) ratio of 1:4, and the mixture was then dissolved in dimethylformamide (Sigma–Aldrich Inc., USA) at a concentration of 18% (w/v) at 45 °C. The polymer solution was drop-casted onto a slide and the resulting film was immersed in deionized water to dissolve NaCl particles and create a porous PCL film (thickness: 350  $\mu\text{m}$ ; size: 4.7 mm  $\times$  10 mm). A small amount of  $\text{CHCl}_3$  was applied to glue the porous PCL and PLLA-PTMC films together to achieve a bilayer structure. N-type Si membranes were subsequently transferred onto the PLLA-PTMC layer of the bilayer structure to achieve conductive paths aligned with the direction of tissue growth. To obtain electrospun directional PCL fibers on top of N-type Si membranes, PCL was dissolved in hexafluoroisopropanol (Shanghai Aladdin Biochemical Co. Ltd., China) with a ratio of 1:10 (w/v). The polymer solution was loaded into a 10 mL syringe with a metallic needle, a high voltage of 15 kV was applied between the needle and the metallic rolling receiver, and the syringe was pushed forward at a speed of 0.3 mm/min. After 30 min, a directional electrospun film (thickness,  $\approx 30 \mu\text{m}$ ) was realized, and the film was then cut into squares ( $\approx 4.7 \text{ mm} \times 10 \text{ mm}$ ). A 3D bioresorbable and conductive nerve scaffold was achieved by rolling the aforementioned multilayer planar structure around a needle (1.5  $\mu\text{m}$  in diameter). To stabilize the structure, a biodegradable suture (poly(glycolic acid), PGA) was wrapped around the scaffold.

**Characterizations of Materials Properties:** A field-emission scanning electron microscopy (SEM) system (Zeiss, Belin, Germany) was used to investigate the morphology of the material surface. Degradation experiments were performed by immersing the conductive scaffold without the electrospun PCL layer (in the planar structure) in PBS solution (replaced everyday) at 55 °C using a water bath, and optical microscope was used to take images at various stages. The SOI was immersed in a PBS solution at 55 °C, with daily replacement of the PBS solution. The device layer thickness of the SOI was periodically measured by profilometry, and its resistance was measured at regular intervals.

**In Vitro Cell Experiments:** The extraction procedure of DRG neurons was as described previously.<sup>[48]</sup> Briefly, SD rats were sacrificed and sterilized by immersing in 75% ethanol for 15 min. DRG neurons were then removed from the intervertebral foramina under a stereomicroscope and isolated using pancreatic enzymes. N-type Si and glass (N-type group and control group) were coated with poly-D-lysine (A38904-01, Gibco) working solutions at 37 °C for 3 h before DRG implantation and rinsed in PBS three times. Isolated DRG neurons were inoculated on the surface of N-type Si (SOI wafer) and glass with 2.5 mL DRG culture medium (Dulbecco's Modified Eagle Medium/Nutrient Mixture F-12 [DMEM/F-12], 2 mM GlutalMAX-1, 1% penicillin–streptomycin, and 1% B-27 factor), and incubated at 37 °C with 5%  $\text{CO}_2$  for 7 days ( $n = 3$ ). DRG neurons were fixed in 4% paraformaldehyde solution for 10 min, and then were rinsed in PBS, followed by incubation in goat serum working solution (10%, Solarbio, China) for 30 min. Next, cells were incubated with mouse anti-NF200 antibodies (Sigma–Aldrich, USA) and rabbit anti-S100 antibodies (Sigma–Aldrich, USA) overnight at 4 °C. The next day, the cells were rinsed with PBS and incubated in secondary antibody working solution (goat anti-rabbit antibodies, Alexa Fluor 594, Abcam, USA, and goat anti-mouse antibodies, Alexa Fluor 488, Abcam, USA) for 2 h at 24 °C. Further, the samples were rinsed three times with PBS, nuclei were stained with 4, 6-diamidino-2-phenylindole (DAPI, 1:200, 4A Biotech, China), sealed with an aqueous sealer, and photographed using a laser confocal microscope (LSM780, Zeiss, Germany).

Schwann cells were derived from SD rat by a modified extraction procedure.<sup>[49]</sup> The obtained Schwann cells were then cultured on N-type Si (SOI wafer) and TCPS (control group) at a density of 5000 cells  $\text{cm}^{-2}$  ( $n = 4$ ). The proliferation of Schwann cells was investigated after 24 and 72 h of culturing. Schwann cells were incubated with rabbit anti-S100 antibodies (Sigma–Aldrich, USA) overnight at 4 °C. The next day, the cells were rinsed with PBS and incubated in secondary antibody working solution (goat anti-rabbit antibodies, Alexa Fluor 594, Abcam, USA) and phalloidin FITC (Sigma–Aldrich, USA) for 2 h at 24 °C. Further, the samples were rinsed three times with PBS, nuclei were stained with 4, 6-diamidino-2-phenylindole (DAPI, 1:200, 4A Biotech, China), sealed with an aqueous sealer, and photographed using a laser confocal microscope (LSM780, Zeiss, Germany). Cell viability was evaluated using Alamar Blue cell viability detection reagent (A50101, Invitrogen, USA). Fluorescence spectrophotometer was used to measure the fluorescent intensity at an excitation wavelength of 560 nm and emission wavelength of 590 nm. Transcriptomic assay was also performed on Schwann cells to investigate the influence of N-type Si. After Schwann cells were cultured 72 h on N-type Si and TCPS, three biological replicates were set up for each group ( $n = 3$ ), and up to 1 million cells were achieved on each sample. Cells were lysed with TRIzol reagent (15 596 018, Life Technologies, USA) for 10 min, snap-frozen in liquid nitrogen, stored at  $-80 \text{ }^\circ\text{C}$ , and transported on dry ice. Subsequent library construction, transcriptome data collection, and analysis were performed by Novogene Co. Ltd. (Beijing, China). Briefly, the total amount and integrity of ribonucleic acid (RNA) were measured using an Agilent 2100 Bioanalyzer after RNA extraction. Subsequently, library construction and quality control assessment were performed, and Illumina NovaSeq 6000 sequencing was performed after passing the quality control test. The quality control data was compared with the reference genome, followed by quantification of gene expression levels and analysis of differential gene expression between the two comparative combinations using the DESeq2 software (1.20.0). Further,  $\text{padj} \leq 0.05$  and  $\log_2(\text{fold change}) \geq 1$  were set as the threshold for significant differential expression. GO and Kyoto Encyclopedia of Genes and Genomes (KEGG) pathway enrichment analysis of differentially expressed genes were performed using the clusterProfiler (3.8.1) software.

**Calcium Imaging of DRG Neurons:** DRG neurons cultured for a week were incubated 30 min in loading solution and then washed twice (2 min each time) in recording solution. The recording solution was a mixture of 145 mM NaCl, 3.6 mM KCl, 1.3 mM  $\text{CaCl}_2$ , 10 mM H-Hepes, and 10 mM glucose. Loading solution was obtained by adding 5  $\mu\text{M}$  Fluo-8 AM (AAT Bioquest, Sunnyvale, CA, USA) in the recording solution. The neurons were then transferred to a recording chamber and recorded using a fluorescence microscope (BX51WI, Olympus, Tokyo, Japan) equipped with a

60x water-immersion objective. By controlling the fluorescent light source (Lambda HPX-L5, Sutter Instrument, Novato, CA, USA), exposures were made at 5-s intervals for 50 ms each time. 10 axons were selected from each group of DRG neurons, and the firing number in 120 s was counted.

**Animal Surgery:** The experimental protocol was approved by the Experimental Animal Ethics Committee of PLA General Hospital (approval number: 2016-x9-07). All procedures related to animal studies were in accordance with the institutional guidelines of the PLA General Hospital. Female SD rats were weighed, intraperitoneally anesthetized with 30 mg kg<sup>-1</sup> pentobarbital sodium, and the right sciatic nerve was exposed by complete dissection in a sterile environment. The sciatic nerve was cut and a 10 mm nerve defect was created. Three groups of scaffolds including the conductive conduit with N-type Si membranes (N-type group), conduit without Si membranes (control) and autograft groups were investigated ( $n = 11$  for each group). All the implants were fixed to the nerve stumps with tension-free sutures under an operating microscope with 8-0 band sutures. The autologous nerve grafting was achieved by rotating the resected 10 mm sciatic nerve. After adequate hemostasis, the muscle layer and skin were closed layer-by-layer with 4-0 surgical sutures, and the incision was disinfected with iodophor. The animals were housed in plastic cages with an automatic water supply and 12 h light/dark cycle.

**Gait Analysis:** Animal gait analyzer (CatWalk, Noldus, China) was used on weeks 3 ( $n = 11$  for each group), 6 ( $n = 6$  for each group), 9 ( $n = 6$  for each group), and 12 ( $n = 6$  for each group) to evaluate motor function recovery. Footprints were photographed for each group. CatWalk XT 10.6 (Noldus, China) software was used to calculate SFI, which was based on the footprints of SD rats. Three parameters of the footprints on the injured side (E) and normal side (N) were measured separately to collect toe width (TS), intermediate toe width (ITS), and footprint length (PL), and the SFI values were calculated by the Bain formula:

$$SFI = 109.5 \times (ETS - NTS) / NTS - 38.3 \times (EPL - NPL) / NPL + 13.3 \times (EIT - NIT) / NIT - 8.8 \quad (1)$$

**Electrophysiology:** Twelve weeks postimplantation, rats were weighed and intraperitoneally anesthetized with 30 mg kg<sup>-1</sup> pentobarbital sodium. Complete dissection was performed to expose the right nerve bridge as well as the normal sciatic nerve on the left side. Synergy electromyography (Oxford, USA) stimulating electrodes were placed on the proximal nerve stump, and parallel recording electrodes were placed on the target gastrocnemius muscle. The stimulation current was set to 3 mA, and CMAP was recorded for a single stimulation. The same parameters were tested on the normal left side. The delay time and peak ratio of the CMAP on the injured/unoperated side were analyzed and derived for each group ( $n = 8$ ).

**Evaluation of Tissue Regeneration on Week 3:** The animals in each group ( $n = 5$ ) were sacrificed by intraperitoneal injection of overdosed sodium pentobarbital. The nerve segments were removed, soaked immediately in 4% paraformaldehyde of 10 times the volume of the sample, and fixed at 4 °C for 24 h. The samples were dehydrated in sunken sugar, embedded in optimal cutting temperature compound gel, and snap-frozen in liquid nitrogen. The nerve grafts were cut into longitudinal sections (10 μm), and stained with NF-200, S-100, and DAPI, and observed by a confocal panoramic scanner (Pannoramic, 3DHISTECH, Hungary).

**Histological and TEM Evaluation of End-Stage Grafts on Week 12:** The animals ( $n = 6$ ) were sacrificed by intraperitoneal injection of overdosed sodium pentobarbital. 2 mm nerve tissue was obtained from the distal graft. Before sampling, petri dishes with fixative for TEM were prepared in advance, small tissue blocks were removed from the animal body, and put immediately into petri dishes, and cut into small pieces with the size of 1 mm<sup>3</sup> in the fixative. The tissue blocks were transferred into an epoxy resin (EP) tube with fresh TEM fixative for further fixation, which was fixed at 4 °C for preservation and transportation. The tissues were washed by 0.1 M PBS (pH 7.4) for three times, 15 min for each wash. After post-fixation, dehydration, Resin penetration and embedding, polymerization treatment, transverse semi-thin sections of nerve segments of 1 μm in thickness were cut using a glass knife in an ultramicrotome (Leica HistoCore Nanocut R, Leica, Germany) and stained with Toluidine Blue dye

(1% in sodium borate, G1032, Servicebio, China) and photographed using a confocal panoramic scanner (Pannoramic, 3DHISTECH, Hungary). Ten randomly selected fields in each group at 60x magnification were captured to quantify the mean density of myelinated nerve fibers by Image ProPlus. Transverse ultrathin sections of nerve segments (thickness: 70 nm) were cut by a diamond knife in an ultramicrotome (Leica HistoCore Nanocut R, Leica, Germany) and collected in copper slot grids with pioloform/carbon support films. The ultrathin sections were counterstained with 3% lead citrate and uranyl acetate, and observed by TEM (CM-120, PHILIPS, Netherlands). Ten randomly selected fields for each group at 3000x magnification were captured to quantify the mean diameter of myelinated nerve fibers and the mean thickness of the myelin sheath by ImageJ.

**Evaluation of End-Stage Target Muscle Recovery:** Both sides of the gastrocnemius muscle were excised under anesthesia and the rats were sacrificed with an intraperitoneal injection of excessive amount of sodium pentobarbital. The sections were then weighed, photographed, and placed in 4% paraformaldehyde fixative of 10 times the volume of the sample for 48 h at 4 °C. After complete fixation of the gastrocnemius muscle in each group, the muscle was dehydrated and embedded, and transverse paraffin sections were prepared. The sections were dewaxed using water and stained according to the instructions of the Masson staining kit (G1006, Servicebio, China). After transparent sealing, images were captured using a panoramic scanning microscope (Pannoramic, 3DHISTECH, Hungary).

**Statistical Data Analysis:** Data are given as mean ± SD. Data were statistically analyzed by the SPSS software package (version 23.0), accompanied by one-way analysis of variance (ANOVA) (\*  $p < 0.05$ , \*\*  $p < 0.01$ ).

## Supporting Information

Supporting Information is available from the Wiley Online Library or from the author.

## Acknowledgements

P.S., Y.G., and C.Y. contributed equally to this work. This study was supported by the National Natural Science Foundation of China (52171239 and T2122010 to L.Y., 52272277 to X.S.), Open Funding Project of the State Key Laboratory of Biochemical Engineering (to L.Y.), and Beijing Municipal Natural Science Foundation (Z220015).

## Conflict of Interest

The authors declare no conflict of interest.

## Data Availability Statement

All data needed to evaluate the conclusions in the paper are present in the paper and/or the Supplementary Materials.

## Keywords

bioresorbable conductive scaffolds, peripheral nerve regeneration, silicon membranes

Received: June 12, 2023  
Revised: September 3, 2023  
Published online: October 15, 2023

- [1] a) J. H. A. Bell, J. W. Haycock, *Tissue Eng Part B Rev* **2012**, *18*, 116; b) U. Kovačič, J. Sketelj, F. F. Bajrović, *Int Rev Neurobiol* **2009**, *87*, 465.

- [2] P.-N. Mohanna, R. C. Young, M. Wiberg, G. Terenghi, *J Anat* **2003**, *203*, 553.
- [3] J. L. Kelsey, *Upper Extremity Disorders: Frequency, Impact, and Cost*, Churchill Livingstone, New York **1997**.
- [4] K. Brattain, *Analysis of the Peripheral Nerve Repair Market in the United States*, Magellan Medical Technology Consultants, Inc, Minneapolis, MN, USA **2013**.
- [5] a) W. Z. Ray, S. E. Mackinnon, *Exp Neurol* **2010**, *223*, 77; b) Y. Gao, Y.-L. Wang, D. Kong, B. Qu, X.-J. Su, H. Li, H.-Y. Pi, *Neural Regener. Res.* **2015**, *10*, 1003.
- [6] S. Kehoe, X. F. Zhang, D. Boyd, *Injury* **2012**, *43*, 553.
- [7] a) G. R. D. Evans, K. Brandt, S. Katz, P. Chauvin, L. Otto, M. Bogle, B. Wang, R. K. Meszlenyi, L. Lu, A. G. Mikos, C. W. Patrick, *Biomaterials* **2002**, *23*, 841; b) D. Arslantunali, T. Dursun, D. Yucel, N. Hasirci, V. Hasirci, *Med. Devices: Evidence Res.* **2014**, *7*, 405.
- [8] a) A. R. Dixon, S. H. Jariwala, Z. Bilis, J. R. Loverde, P. F. Pasquina, L. M. Alvarez, *Biomaterials* **2018**, *186*, 44; b) Y. Niu, K. C. Chen, T. He, W. Yu, S. Huang, K. Xu, *Biomaterials* **2014**, *35*, 4266.
- [9] a) M.-H. Beigi, L. Ghasemi-Mobarakeh, M. P. Prabhakaran, K. Karbalaie, H. Azadeh, S. Ramakrishna, H. Baharvand, M.-H. Nasr-Esfahani, M.-H. Nasr-Esfahani, *J. Biomed. Mater. Res., Part A* **2021**, *109*, 572; b) L. N. Novikova, J. Pettersson, M. Brohlin, M. Wiberg, L. N. Novikov, *Biomaterials* **2008**, *29*, 1198.
- [10] T. Gordon, A. W. English, *Eur J Neurosci* **2016**, *43*, 336.
- [11] a) Z. Yahong, L. Yunyun, D. Supeng, Z. Kunyu, M. Hai-quan, Y. Yumin, *Biomaterials* **2020**, *255*, 191; b) J. Koo, M. R. Macewan, S.-K. Kang, S. M. Won, M. Stephen, P. Gamble, Z. Xie, Y. Yan, Y.-Y. Chen, J. Shin, N. Birenbaum, S. Chung, S. B. Kim, J. Khalifeh, D. V. Harburg, K. Bean, M. Paskett, J. Kim, Z. S. Zohny, S. M. Lee, R. Zhang, K. Luo, B. Ji, A. Banks, H. M. Lee, Y. Huang, W. Z. Ray, J. A. Rogers, *Nat. Med.* **2018**, *24*, 1830; c) T. Gordon, *Neurotherapeutics* **2016**, *13*, 295; d) W. Wang, W. Liu, H. Zhu, F. Li, Y. Wo, W. Shi, X. Fan, W. Ding, *Cell. Mol. Neurobiol.* **2011**, *31*, 459; e) L. Wang, C. Lu, S. Yang, P. Sun, Y. Wang, Y. Guan, S. Liu, D. Cheng, H. Meng, Q. Wang, J. He, H. Hou, H. Li, W. Lu, Y. Zhao, J. Wang, Y. Zhu, Y. Li, D. Luo, T. Li, H. Chen, S. Wang, X. Sheng, W. Xiong, X. Wang, J. Peng, L. Yin, *Sci. Adv.* **2020**, *6*, eabc6686; f) J. Huang, Y. Zhang, L. Lu, X. Hu, Z. Luo, *Eur J Neurosci* **2013**, *38*, 3691; g) Z. Liu, X. Wan, Z. L. Wang, L. Li, *Adv. Mater.* **2021**, *33*, 2007429.
- [12] a) Y. Sun, Q. Quan, H. Meng, Y. Zheng, J. Peng, Y. Hu, Z. Feng, X. Sang, K. Qiao, W. He, X. Chi, L. Zhao, *Adv. Healthcare Mater.* **2019**, *8*, e1900127; b) L. Li, D. Li, Y. Wang, T. Ye, E. He, Y. Jiao, L. Wang, F. Li, Y. Li, J. Ding, K. Liu, J. Ren, Q. Li, J. Ji, Y. Zhang, *Adv. Mater.* **2023**, *35*, 2302997; c) J. Huang, L. Lu, J. Zhang, X. Hu, Y. Zhang, W. Liang, S. Wu, Z. Luo, *PLoS One* **2012**, *7*, e39526; d) J. Huang, X. Hu, L. Lu, Z. Ye, Y. Wang, Z. Luo, *J Neurotrauma* **2009**, *26*, 1805; e) Jinghui Huang, Lei Lu, Xueyu Hu, Zhengxu Ye, Ye Peng, Xiaodong Yan, Dan Geng, Zhuojing Luo, *Neurorehabil Neural Repair* **2010**, *24*, 736.
- [13] a) C. D. Mccaig, A. M. Rajnicek, B. Song, M. Zhao, *Physiol. Rev.* **2005**, *85*, 943; b) L. Cao, D. Wei, B. Reid, S. Zhao, J. Pu, T. Pan, E. N. Yamoah, M. Zhao, *EMBO Rep.* **2013**, *14*, 184; c) A. Casella, A. Panitch, J. K. Leach, *Bioelectricity* **2021**, *3*, 27; d) P. Zarrintaj, E. Zangene, S. Manouchehri, L. M. Amirabad, N. Baheiraei, M. R. Hadjighasem, M. Farokhi, M. R. Ganjali, B. W. Walker, M. R. Saeb, M. Mozafari, S. Thomas, N. Annabi, *Appl Mater Today* **2020**, *20*, 100784.
- [14] Y. Zhao, J. Liu, Y. Gao, Z. Xu, C. Dai, G. Li, C. Sun, Y. Yang, K. Zhang, *J. Mater. Chem. B* **2022**, *10*, 1582.
- [15] a) R. Ravichandran, S. Sundarajan, J. R. Venugopal, S. Mukherjee, S. Ramakrishna, *J R Soc Interface* **2010**, *7*, S559; b) M. R. Abidian, J. M. Corey, D. R. Kipke, D. C. Martin, *Small* **2010**, *6*, 421.
- [16] R. Guo, S. Zhang, M. Xiao, F. Qian, Z. He, D. Li, X. Zhang, H. Li, X. Yang, M. Wang, R. Chai, M. Tang, *Biomaterials* **2016**, *106*, 193.
- [17] B. F. Liu, J. Ma, Q. Y. Xu, F. Z. Cui, *Colloids Surf., B* **2006**, *53*, 175.
- [18] a) S. Meng, *Tissue Eng. Regener. Med.* **2014**, *11*, 274; b) S. K. Seidlits, J. Y. Lee, C. E. Schmidt, *Nanomedicine* **2008**, *3*, 183; c) A. Fraczek-Szczypta, *Mater. Sci. Eng. C* **2014**, *34*, 35.
- [19] a) L. Wang, Q. Huang, J.-Y. Wang, *Langmuir* **2015**, *31*, 12315; b) L. Ouyang, C.-C. Kuo, B. Farrell, S. Pathak, B. Wei, J. Qu, D. C. Martin, *J. Mater. Chem. B* **2015**, *3*, 5010; c) J. Y. Lee, C. A. Bashur, A. S. Goldstein, C. E. Schmidt, *Biomaterials* **2009**, *30*, 4325.
- [20] W. Jing, Q. Ao, L. Wang, Z. Huang, Q. Cai, G. Chen, X. Yang, W. Zhong, *Chem. Eng. J.* **2018**, *345*, 566.
- [21] M. R. Abidian, E. D. Daneshvar, B. M. Egeland, D. R. Kipke, P. S. Cederna, M. G. Urbanek, *Adv. Healthcare Mater.* **2012**, *1*, 762.
- [22] J. Park, J. Jeon, B. Kim, M. S. Lee, S. Park, J. Lim, J. Yi, H. Lee, H. S. Yang, J. Y. Lee, *Adv. Funct. Mater.* **2020**, *30*, 2003759.
- [23] S. Ghosh, S. Haldar, S. Gupta, A. Bisht, S. Chauhan, V. Kumar, P. Roy, D. Lahiri, *ACS Appl Bio Mater* **2020**, *3*, 5796.
- [24] a) L. Wang, Y. Gao, F. Dai, D. Kong, H. Wang, P. Sun, Z. Shi, X. Sheng, B. Xu, L. Yin, *ACS Appl. Mater. Interfaces* **2019**, *11*, 18013; b) Y. K. Lee, K. J. Yu, E. Song, A. Barati Farimani, F. Vitale, Z. Xie, Y. Yoon, Y. Kim, A. Richardson, H. Luan, Y. Wu, X. Xie, T. H. Lucas, K. Crawford, Y. Mei, X. Feng, Y. Huang, B. Litt, N. R. Aluru, L. Yin, J. A. Rogers, *ACS Nano* **2017**, *11*, 12562; c) S.-W. Hwang, H. Tao, D.-H. Kim, H. Cheng, J.-K. Song, E. Rill, M. A. Brenckle, B. Panilaitis, S. M. Won, Y.-S. Kim, Y. M. Song, K. J. Yu, A. Ameen, R. Li, Y. Su, M. Yang, D. L. Kaplan, M. R. Zakin, M. J. Slepian, Y. Huang, F. G. Omenetto, J. A. Rogers, *Science* **2012**, *337*, 1640.
- [25] J. D. Rimstidt, H. L. Barnes, *Geochim. Cosmochim. Acta* **1980**, *44*, 1683.
- [26] J. D. Birchall, J. S. Chappell, *Clin. Chem.* **1988**, *34*, 265.
- [27] a) C. Coletti, M. Jaroszeski, A. Pallao, A. Hoff, S. Iannotta, S. Saddow, presented at Conf. Proc. IEEE Eng. Med. Biol. Soc., Lyon, France **2007**, *8*; b) W. Bai, J. Shin, R. Fu, I. Kandela, D. Lu, X. Ni, Y. Park, Z. Liu, T. Hang, D. Wu, Y. Liu, C. R. Haney, I. Stepien, Q. Yang, J. Zhao, K. R. Nandoliya, H. Zhang, X. Sheng, L. Yin, K. Macrenaris, A. Brikha, F. Aird, M. Pezhouh, J. Hornick, W. Zhou, J. A. Rogers, *Nat. Biomed. Eng.* **2019**, *3*, 644.
- [28] J.-H. Park, L. Gu, G. Von Maltzahn, E. Ruoslahti, S. N. Bhatia, M. J. Sailor, *Nat Mater* **2009**, *8*, 331.
- [29] a) J. F. Poplewell, S. J. King, J. P. Day, P. Ackrill, L. K. Fifield, R. G. Cresswell, M. L. Di Tada, K. Liu, *J. Inorg. Biochem.* **1998**, *69*, 177; b) E. M. Carlisle, *Science* **1970**, *167*, 279; c) R. Jugdaohsingh, *J Nutr Health Aging* **2007**, *11*, 99.
- [30] M. Park, E. Oh, J. Seo, M.-H. Kim, H. Cho, J. Y. Choi, H. Lee, I. S. Choi, *Small* **2016**, *12*, 1148.
- [31] G. Kaur, R. Adhikari, P. Cass, M. Bown, P. Gunatillake, *RSC Adv.* **2015**, *5*, 37553.
- [32] a) Y. Bledi, A. J. Domb, M. Linial, *Brain Res* **2000**, *5*, 282; b) S. Lakard, G. Herlem, A. Propper, A. Kastner, G. Michel, N. Vallès-Villarreal, T. Gharbi, B. Fahys, *Bioelectrochemistry* **2004**, *62*, 19.
- [33] a) M. Mattotti, L. Micholt, D. Braeken, D. Kovacic, *J. Neural Eng.* **2015**, *12*, 026001; b) H. Claire Yu-Mei, Z. Chuansheng, R. Z. Daniel, L. Christophe, N. R. Matthew, *J Neurosci Res* **2017**, *37*, 11323.
- [34] C. Cheng, D. W. Zochodne, *Neuroscience* **2002**, *115*, 321.
- [35] a) Y. Huang, Y. Cui, H. Deng, J. Wang, R. Hong, S. Hu, H. Hou, Y. Dong, H. Wang, J. Chen, L. Li, Y. Xie, P. Sun, X. Fu, L. Yin, W. Xiong, S.-H. Shi, M. Luo, S. Wang, X. Li, X. Sheng, *Nat. Biomed. Eng.* **2022**, *7*, 486; b) A. Prominski, J. Shi, P. Li, J. Yue, Y. Lin, J. Park, B. Tian, M. Y. Rotenberg, *Nat Mater* **2022**, *21*, 647; c) M. Silverá Ejebe, M. Jakesová, J. J. Ferrero, L. Migliaccio, I. Sahalianov, Z. Zhao, M. Berggren, D. Khodagholy, V. Derek, J. N. Gelinas, E. D. Glowacki, *Nat. Biomed. Eng.* **2022**, *6*, 741.
- [36] a) H. Xu, J. M. Holzwarth, Y. Yan, P. Xu, H. Zheng, Y. Yin, S. Li, P. X. Ma, *Biomaterials* **2014**, *35*, 225; b) A. Escobar, A. Serafin, M. R. Carvalho, M. Culebras, A. Cantarero, A. Beaucamp, R. L. Reis, J. M. Oliveira, M. N. Collins, *Adv. Compos. Mater.* **2023**, *6*, 118.

- [37] S.-W. Hwang, G. Park, H. Cheng, J.-K. Song, S.-K. Kang, L. Yin, J.-H. Kim, F. G. Omenetto, Y. Huang, K.-M. Lee, J. A. Rogers, *Adv Mater* **2014**, *26*, 1992.
- [38] a) Y. W. Fan, F. Z. Cui, S. P. Hou, Q. Y. Xu, L. N. Chen, I.-S. Lee, *J Neurosci Methods* **2002**, *120*, 17; b) J. Wang, L. Ren, L. Li, W. Liu, J. Zhou, W. Yu, D. Tong, S. Chen, *Lab Chip* **2009**, *9*, 644.
- [39] J. Henley, M.-M. Poo, *Trends Cell Biol.* **2004**, *14*, 320.
- [40] a) R. W. Gunderson, J. N. Barrett, *J. Cell Biol.* **1980**, *87*, 546; b) R. S. Bedlack, M.-D. Wei, L. M. Loew, *Neuron* **1992**, *9*, 393.
- [41] J. Marczak, M. Kargol, M. Psarski, G. Celichowski, *Appl. Surf. Sci.* **2016**, *380*, 91.
- [42] Y. Qian, H. Lin, Z. Yan, J. Shi, C. Fan, *Mater. Today.* **2021**, *51*, 165.
- [43] S. E. Mackinnon, *Plast. Reconstr. Surg.* **1996**, *98*, 1272.
- [44] S. Raimondo, M. Fornaro, F. Di Scipio, G. Ronchi, M. G. Giacobini-Robecchi, S. Geuna, *Int Rev Neurobiol* **2009**, *87*, 81.
- [45] S.-K. Kang, R. K. J. Murphy, S.-W. Hwang, S. M. Lee, D. V. Harburg, N. A. Krueger, J. Shin, P. Gamble, H. Cheng, S. Yu, Z. Liu, J. G. Mccall, M. Stephen, H. Ying, J. Kim, G. Park, R. C Webb, C. H. Lee, S. Chung, D. S. Wie, A. D. Gujar, B. Vemulapalli, A. H. Kim, K.-M. Lee, J. Cheng, Y. Huang, S. H. Lee, P. V. Braun, W. Z. Ray, J. A. Rogers, *Nature* **2016**, *530*, 71.
- [46] a) W. Duan, X. Liu, J. Zhao, Y. Zheng, J. Wu, *ACS Appl Mater Interfaces* **2022**, *14*, 48368; b) M. Cui, S. Liu, B. Song, D. Guo, J. Wang, G. Hu, Y. Su, Y. He, *Nanomicro Lett* **2019**, *11*, 73.
- [47] Y. Jiang, X. Li, B. Liu, J. Yi, Y. Fang, F. Shi, X. Gao, E. Sudzilovsky, R. Parameswaran, K. Koehler, V. Nair, J. Yue, K. Guo, Y. Fang, H.-M. Tsai, G. Freyermuth, R. C. S. Wong, C.-M. Kao, C.-T. Chen, A. W. Nicholls, X. Wu, G. M. G. Shepherd, B. Tian, *Nat. Biomed. Eng.* **2018**, *2*, 508.
- [48] X. Sun, Y. Wang, Z. Guo, B. Xiao, Z. Sun, H. Yin, H. Meng, X. Sui, Q. Zhao, Q. Guo, A. Wang, W. Xu, S. Liu, Y. Li, S. Lu, J. Peng, *Adv Healthcare Mater.* **2018**, *7*.
- [49] P. Maurel, in *Schwann Cells: Methods and Protocols*, Humana, New York, USA **2018**.

# ADVANCED HEALTHCARE MATERIALS

## Supporting Information

for *Adv. Healthcare Mater.*, DOI 10.1002/adhm.202301859

A Bioresorbable and Conductive Scaffold Integrating Silicon Membranes for Peripheral Nerve Regeneration

*Pengcheng Sun, Yanjun Guan, Can Yang, Hanqing Hou, Shuang Liu, Boyao Yang, Xiangling Li, Shengfeng Chen, Liu Wang, Huachun Wang, Yunxiang Huang, Xing Sheng, Jiang Peng, Wei Xiong, Yu Wang\* and Lan Yin\**

# Figure S1

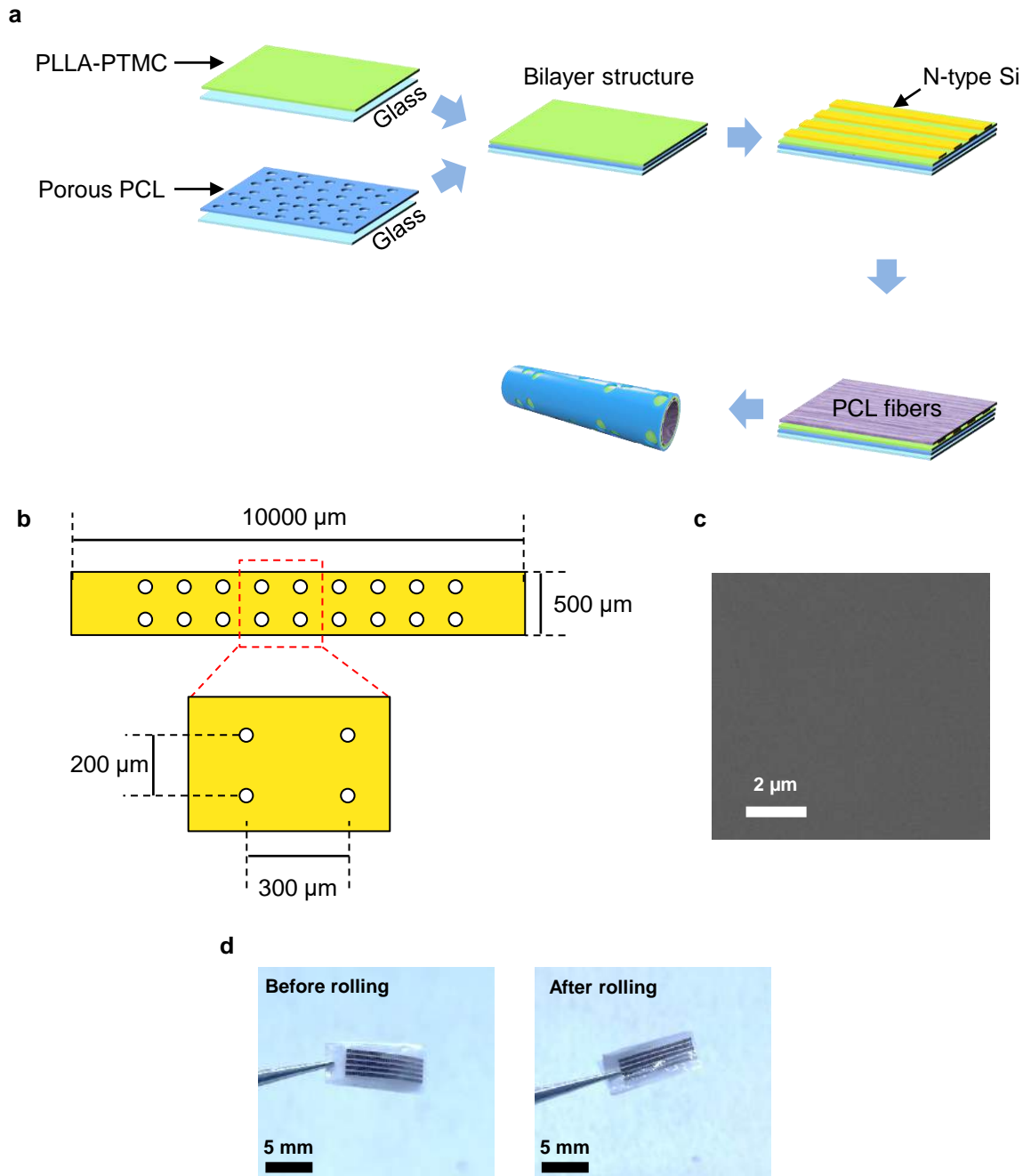


**Fig. S1.** **a**, Fabrication process of the bioresorbable and conductive nerve conduit. **b**, Schematic diagram of the N-Type Si membrane with an array of holes (50  $\mu\text{m}$  in diameter). **c**, SEM image of N-type Si surface. **d**, Optical images of the bioresorbable and conductive nerve conduit (without electrospun PCL fibers) before and after rolling.



# Figure S2

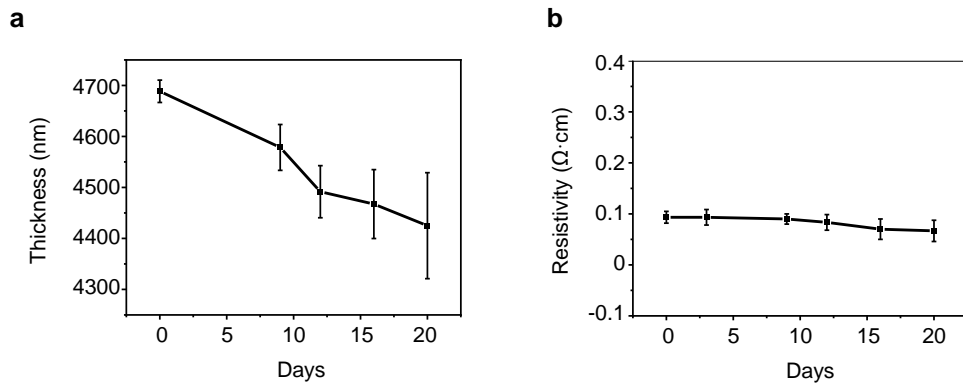


**Fig. S2.** **a**, Changes in film thickness over time after N-type Si films immersed in PBS solution at 55 °C. **b**, Changes in resistivity of N-type Si films immersed in PBS solution at 55 °C over time.

# Figure S3

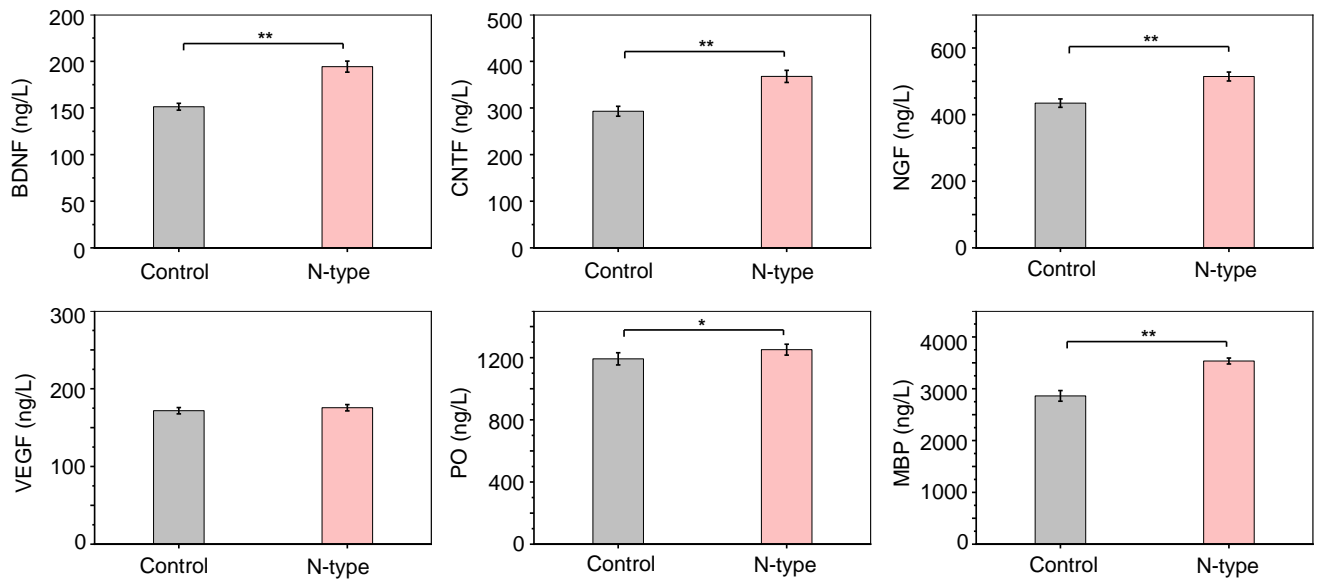


**Fig. S3. The influence of conductive N-type Si on the behavior of Schwann cells.** Enzyme-linked immunosorbent assay (ELISA) of BDNF, CNTF, NGF, VEGF, PO and MBP production in Schwann cells of the N-type and control groups on day 3. n = 4 independent experiments. Data are mean  $\pm$  standard deviation (\* p < 0.05, \*\* p < 0.01).

# Figure S4

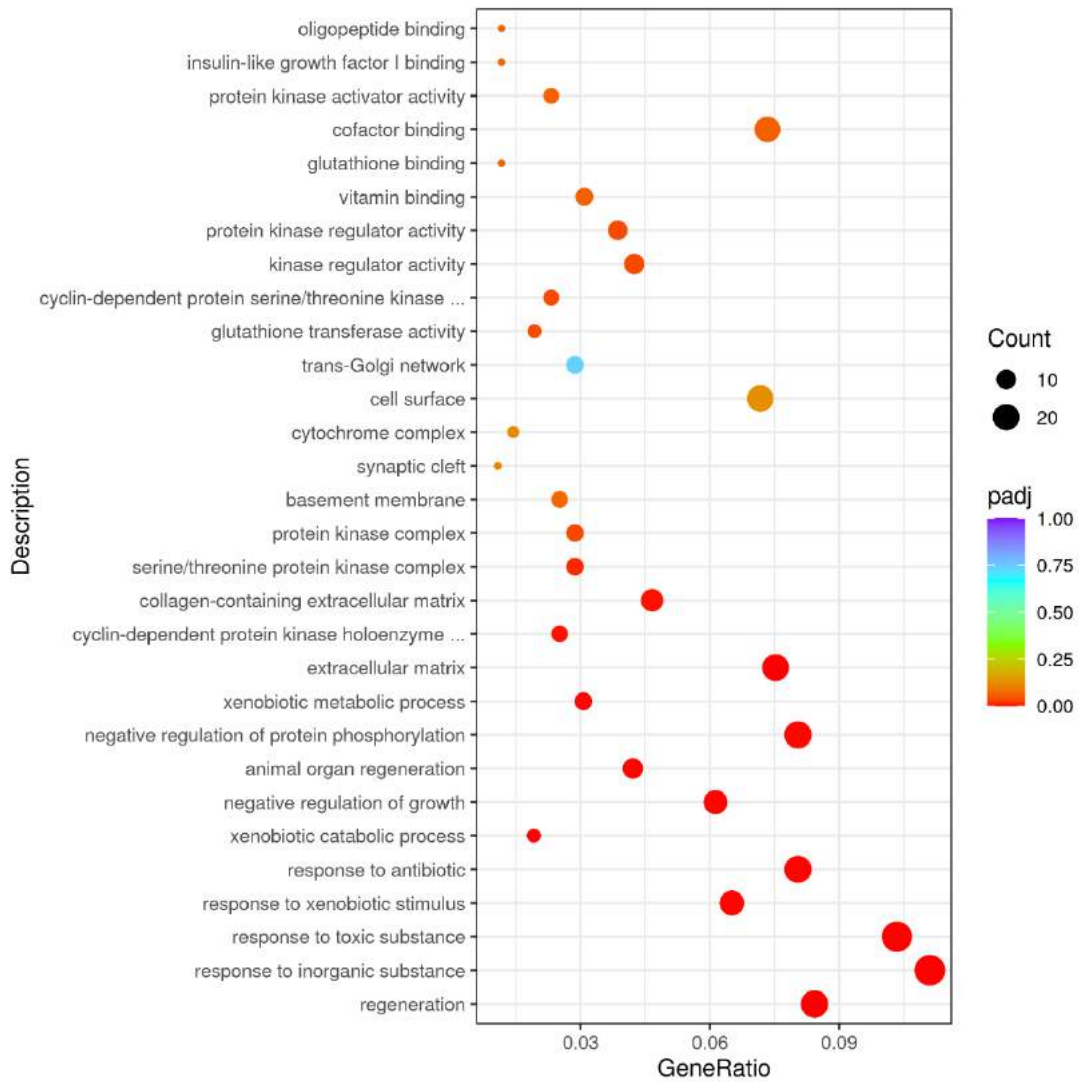


**Fig. S4. GO enrichment analysis of Schwann cells in the N-type group compared with the control group.** 30 categories of genes with the most significant differences between the N-type and control groups are plotted. The horizontal coordinate represents the proportion of genes in each category that demonstrates significant differences, a larger circle area suggests a greater number of genes under that category, and the color of the circles indicates the differences between the two groups, where red suggesting greater differences (significant enrichment) and purple suggesting less differences. n = 3 independent experiments.

## Figure S5

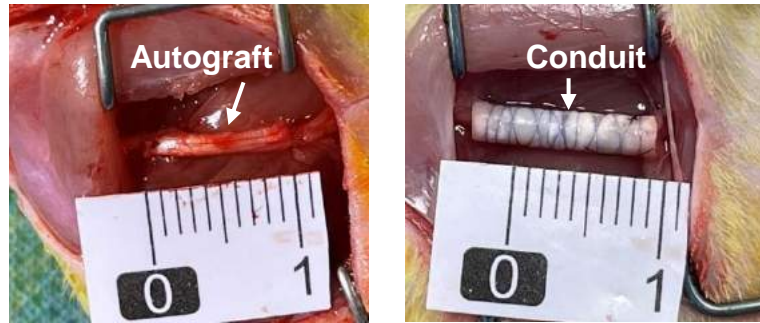


**Fig. S5. Surgical images of the implantation of conductive nerve conduit at the sciatic nerves of SD rats.** Left: Implantation with an autograft. Right: Implantation with a bioresorbable and conductive conduit.

## Figure S6

### Autograft

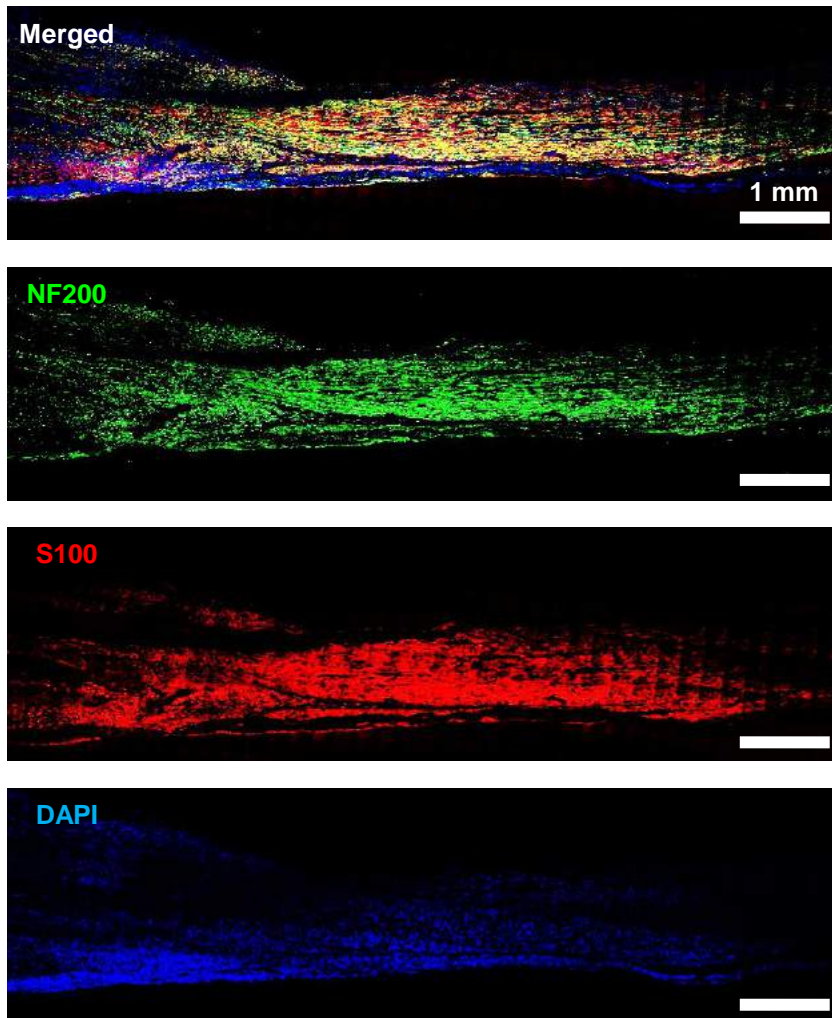


**Fig. S6. Immunofluorescent images of the longitudinal sections of regenerated tissues at 3 weeks postimplantation of the Autograft group.** Immunohistochemical staining: axons (NF200, green), Schwann cells (S100, red), and nuclei (DAPI, blue).

# Figure S7

## Control

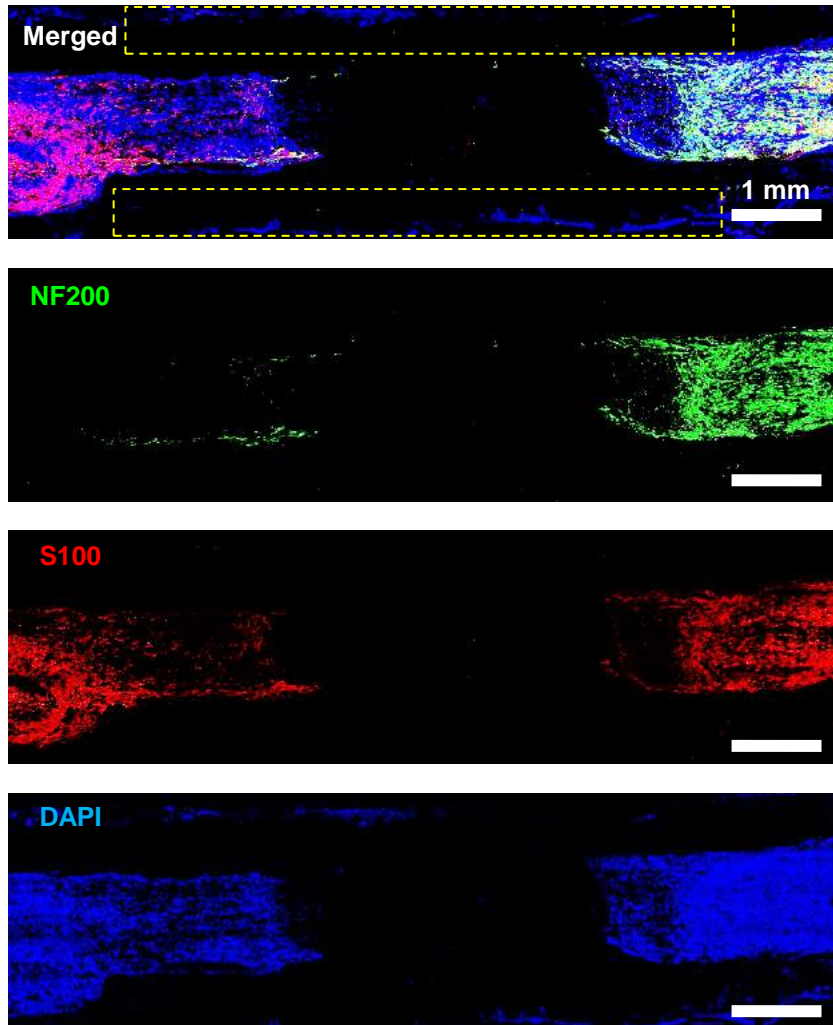


**Fig. S7. Immunofluorescent images of the longitudinal sections of regenerated tissues at 3 weeks postimplantation of the control group.** Immunohistochemical staining: axons (NF200, green), Schwann cells (S100, red), and nuclei (DAPI, blue). The yellow dashed lines represent the contour of the nerve conduits.

# Figure S8

## N-type

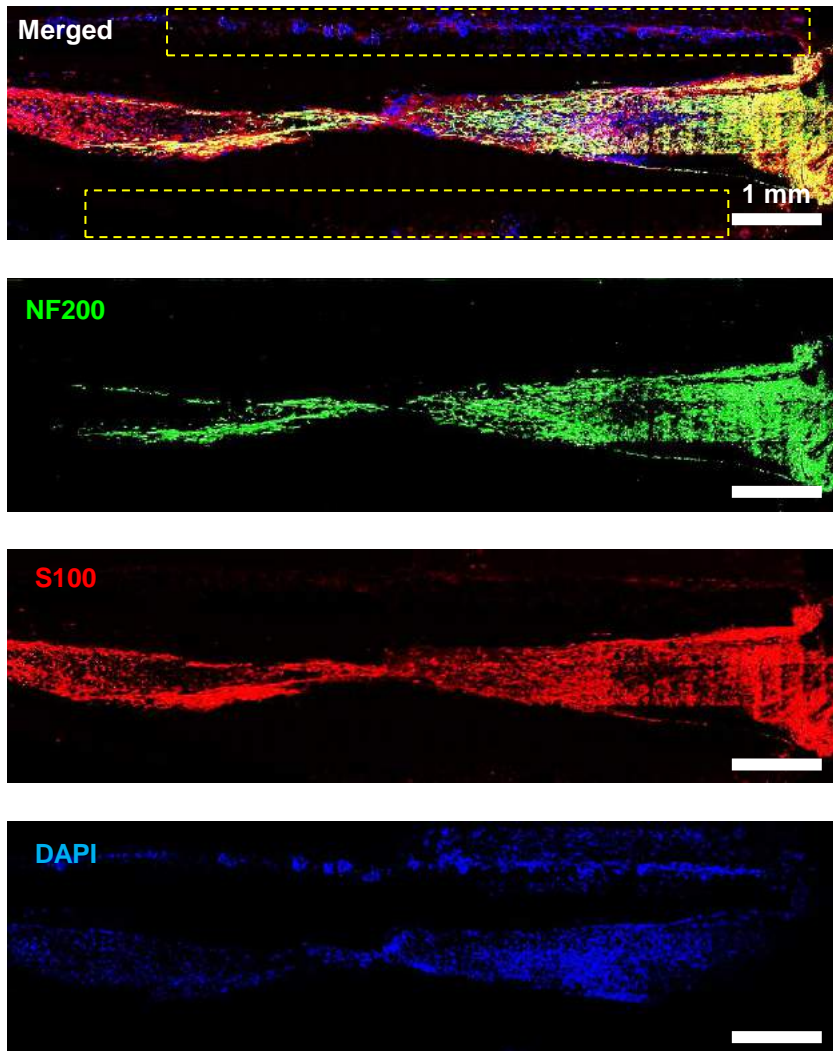


**Fig. S8. Immunofluorescent images of the longitudinal sections of regenerated tissues at 3 weeks postimplantation of the N-type group.** Immunohistochemical staining: axons (NF200, green), Schwann cells (S100, red), and nuclei (DAPI, blue). The yellow dashed lines represent the contour of the nerve conduits.

# Figure S9

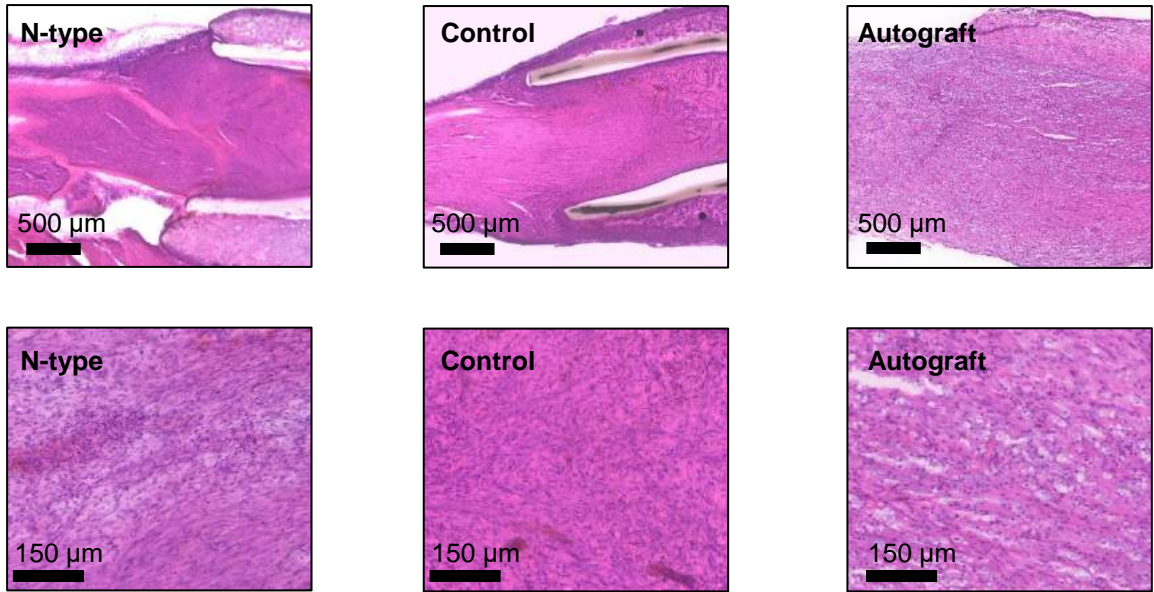


**Fig. S9.** H&E staining images of the longitudinal sections of regenerated tissues at 3 weeks postimplantation.